This is a repository copy of *Fracture and damage in quasi-brittle materials: a comparison of approaches*.

Fracture and damage in quasi-brittle materials: A comparison of approaches

René de Borst

University of Sheffield, Department of Civil and Structural Engineering, Sheffield, S1 3JD, United Kingdom

ARTICLE INFO

ABSTRACT

A overview is given of different approaches to simulate and predict crack propagation in quasi-brittle materials, pointing out their merits, disadvantages and complementarity. Discrete crack approaches, smeared crack approaches and Molecular Dynamics are considered from a historical perspective, and it is discussed in which circumstances they are best used. For the various versions of the discrete and smeared approaches it is shown how the methods within each class have evolved, or why new methods have developed due to shortcomings of earlier versions.

1. Introduction

Fracture lies at the heart of many failures in natural and man-made materials. Fracture mechanics, as a scientific discipline in its own right, originated in the early 20th Century with the pioneering work of Inglis [1] and Griffiths [2]. Driven by some spectacular disasters in the shipbuilding and aerospace industries, and building on the seminal work of Irwin [3], Dugdale [4] and Barenblatt [5] fracture mechanics has become an important tool in the analysis of structural integrity.

Herein, we will focus on methodologies that have been developed for the numerical simulation of fracture initiation and fracture propagation in quasi-brittle materials, such as concrete, rocks, ceramics, and most biomaterials. These materials are heterogeneous from a certain scale upwards, which is usually visible with the naked eye. This is different from, for instance, metals or polymers, where heterogeneity becomes only visible under a microscope or an electron microscope, and where fracture is ductile, i.e. accompanied by significant plastic deformations. It is also different from fracture in brittle materials like glass, an amorphous material, where plastic deformations around the crack tip are practically absent.

1.1. Discrete vs smeared approaches: a long-standing controversy

The numerical simulation of fracture in quasi-brittle materials was initiated in the late 1960s. Two markedly different approaches were pioneered, namely the discrete crack models [6] and the smeared crack models [7]. The discrete crack approach is intuitively appealing: a crack is introduced as a discontinuity in the geometry. Hence, the topology of the body is changing continuously when cracks propagate or when more cracks nucleate. Indeed, the discrete crack model basically aims at simulating the initiation and propagation of a limited number of (clearly) visible cracks.

On the other hand, the smeared crack model is based on the idea that in quasi-brittle materials, due to the heterogeneity which can be observed at a mesoscopic level, and the possible presence of reinforcement such as glass or polymer fibres, or steel bars, many small cracks nucleate which link up only in a later stage to form one or more dominant cracks. Since not each individual crack is resolved the smeared crack model captures the deterioration process through a constitutive relation.

Over the years strong opinions have been expressed regarding both approaches. But some convergence seems to occur. For example, while some form of remeshing is necessary to make discrete crack models work, it turns out that the most recent development within the smeared crack approach, namely the phase-field method for brittle fracture [8–10], requires such dense meshes that some form of remeshing is also necessary in order to keep computing times within acceptable limits, thereby partly removing the original advantage of smeared crack models over discrete approaches [11]. However, differences remain. Three-dimensional implementations are straightforward in smeared approaches and require no special provisions compared to two-dimensional analyses. Also, crack branching is a natural outcome of analyses that use the phase-field approach [12,13]. Indeed, discrete approaches to crack propagation in three dimensions require special crack front capturing techniques and sophisticated data structures, while additional assumptions are needed when attempting to simulate crack branching. The major advantage of discrete approaches still lies in the fact that the crack width is directly available, and the knowledge of this quantity is required in the cohesive-zone approach to fracture, but also in analyses of fracture propagation in fluid-saturated porous media, where the crack width determines the amount of fluid that is transported in the fracture [14].

2. Molecular Dynamics modelling of fracture

All the above considerations pertain to continuum mechanics models. However, modelling at a lower scale, e.g. the simulation of the breakage of bonds at molecular level, have also become en vogue [15–17] and is most useful for building an understanding of fracture processes at microscopic scales. In particular for metals and polymers simulations based on Molecular Dynamics (MD) are essential in upscaling methods, for instance when attempting to construct constitutive models at mesoscopic scales from the physics at lower scales. Therefore, before embarking on a more in-depth discussion of fracture and damage models that are rooted in a continuum description of matter, we will briefly discuss fracture using molecular modelling. We will show a typical example, which demonstrates that crack branching under dynamic loadings is also for this method a natural outcome of the analysis.

2.1. Governing equations for molecular Dynamics

Molecular Dynamics is rooted in the classical Newtonian equations of motion. For an atom i with a mass m_i and position $\mathbf{r}_i$ we have:

$$m_i \ddot{\mathbf{r}}_i = \mathbf{f}_i \tag{1}$$

The force $\mathbf{f}_i$ is the sum of all N inter-atomic contributions $\mathbf{f}_{ij}$, i.e., the force on atom i exerted by atom j

$$\mathbf{f}_i = \sum_{j=1, j \neq i}^{N} \mathbf{f}_{ij} \tag{2}$$

and can be derived from a potential energy function $\mathcal{U}$:

$$\mathbf{f}_i = -\frac{\partial \mathcal{U}(\mathbf{r}_1, \ldots, \mathbf{r}_N)}{\partial \mathbf{r}_i} \tag{3}$$

It is emphasised that the inter-atomic forces are long-range forces and that *all* atoms in the body interact. However, at a certain distance the interaction becomes negligible and a cut-off distance r_c is usually applied beyond which no interaction is taken into account, resulting in just n_i interactions being considered for atom i.

To extract continuum mechanical quantities from atomistic forces we depart from the atomistic stress tensor for atom i, which is a measurement of the inter-atomic interactions of the atom with its neighbours. A widely used stress quantity defined on the atomistic domain is the virial stress, which takes into account the interactions and a kinetic energy contribution [18–20]. Unfortunately, the definitions for the virial stress, while correct in a statistical and thermodynamics sense, do not correspond to the Cauchy stress. However, the part of the virial stress which represents the inter-atomic interactions does reduce to the Cauchy stress, and therefore has a physical meaning. Hence we adopt the following definition for the stress tensor:

$$\boldsymbol{\sigma}_i = \frac{1}{2\mathcal{V}_i} \sum_{r_{ij} < r_c} \mathbf{f}_{ji} \otimes \mathbf{r}_{ij} \tag{4}$$

where $\mathcal{V}_i$ is the volume of the atom i, $\mathbf{r}_{ij} = \mathbf{r}_i - \mathbf{r}_j$, and $r_{ij} = |\mathbf{r}_{ij}|$. Subsequently, the average of this atomistic stress tensor is computed over the volume around i within the cut-off radius r_c. The average or continuum stress at atom i thus reads:

$$\boldsymbol{\sigma}_i{}^{avg} = \frac{1}{n_i} \sum_{j=1}^{n_i} \boldsymbol{\sigma}_j \tag{5}$$

2.2. Relations to other discrete models

The concept of Molecular Dynamics is essentially not different from that in Discrete Element Methods (DEM) [21,22], which are frequently used for failure simulations in granular materials, concrete and rocks. In both approaches classical Newtonian mechanics applies between point masses, the main difference being that the long-range forces which are derived from a potential energy function are replaced by springs
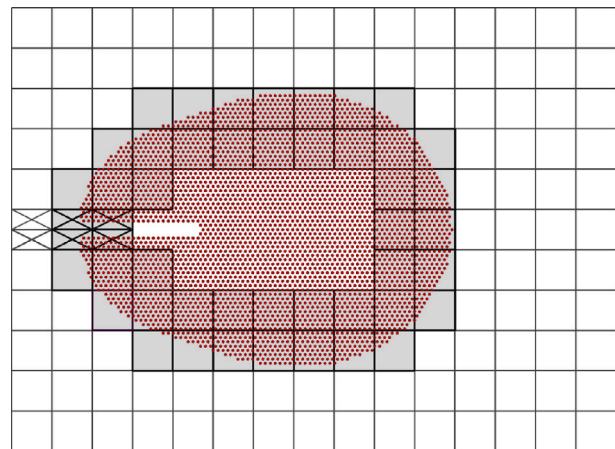

Fig. 1. The dark, 'pear-shaped' area is the domain where an MD calculation is carried out (Ω_m). There is a coupling region Ω_c which consists of elements in grey that are surrounded by a bold line.

between the nearest neighbours, thus returning to the concept of local constitutive relations.

The springs can also be considered as bars with a Young's modulus, which leads to the so-called lattice models [23]. To remedy certain issues the bars in lattice models have later been replaced by beam elements [24], which can then be conceived as a discretised version of the Cosserat continuum [25]. Similar to smeared crack models, a problem with discrete elements and lattice models is the combination with diffusion-like phenomena. In fact, issues already arise when modelling the diffusion phenomenon itself. A possible solution is to use pipe elements to model the flow in a porous medium [26], but it is unclear how such discrete elements can properly model complex flow patterns.

2.3. Coupling of finite element methods and molecular Dynamics

Molecular Dynamics simulations are extremely CPU-intensive, rendering simulations of even just a few square millimetres computationally unfeasible. For this reason the MD simulations are often carried out on a very small domain of interest, which is then coupled to the surrounding body modelled using continuum mechanics and discretised using finite elements or another suitable discretisation method, e.g. [27].

It is possible to couple both domains via a sharp interface, i.e. a line in two dimensions or a plane in three dimensions. However, the long-range forces in the molecular domain can make this less accurate, especially under dynamic loading conditions, when spurious wave reflections may be incurred. For this reason, it is preferable to define a coupling zone between both domains as well as coupling functions which are used to preserve the global energy [28]. A patch of atoms, Ω_m, is then included in the continuum Ω_M at a given position, for instance the pear-shaped, dark patch in Fig. 1, herein named the Molecular Dynamics Box (MD-Box). Subsequently, a coupling zone Ω_c is defined, where the MD-domain and the continuum domain overlap, indicated by the grey zone in the figure. The finite elements in this zone are 'coupling elements'. Inside the MD-Box, where only the atomistic model applies, elements are removed.

For energy conservation the energy is partitioned between both models using the functions $0 \leq \alpha \leq 1$ and $0 \leq \beta \leq 1$, which form a partition of unity, such that:

$$\begin{cases} \alpha(\mathbf{x}) = 1 & \beta(\mathbf{x}) = 0 & \text{for } \mathbf{x} \in \Omega_M \backslash \Omega_c \\ \alpha(\mathbf{x}) = 0 & \beta(\mathbf{x}) = 1 & \text{for } \mathbf{x} \in \Omega_m \backslash \Omega_c \end{cases} \tag{6}$$

Lagrange multipliers can then be used to ensure a velocity coupling in the domain Ω_c [28]. For applications like the example shown below this model can be enhanced such that the MD-Box is tied to the crack tip, i.e. moves with the tip when the crack propagates [29].
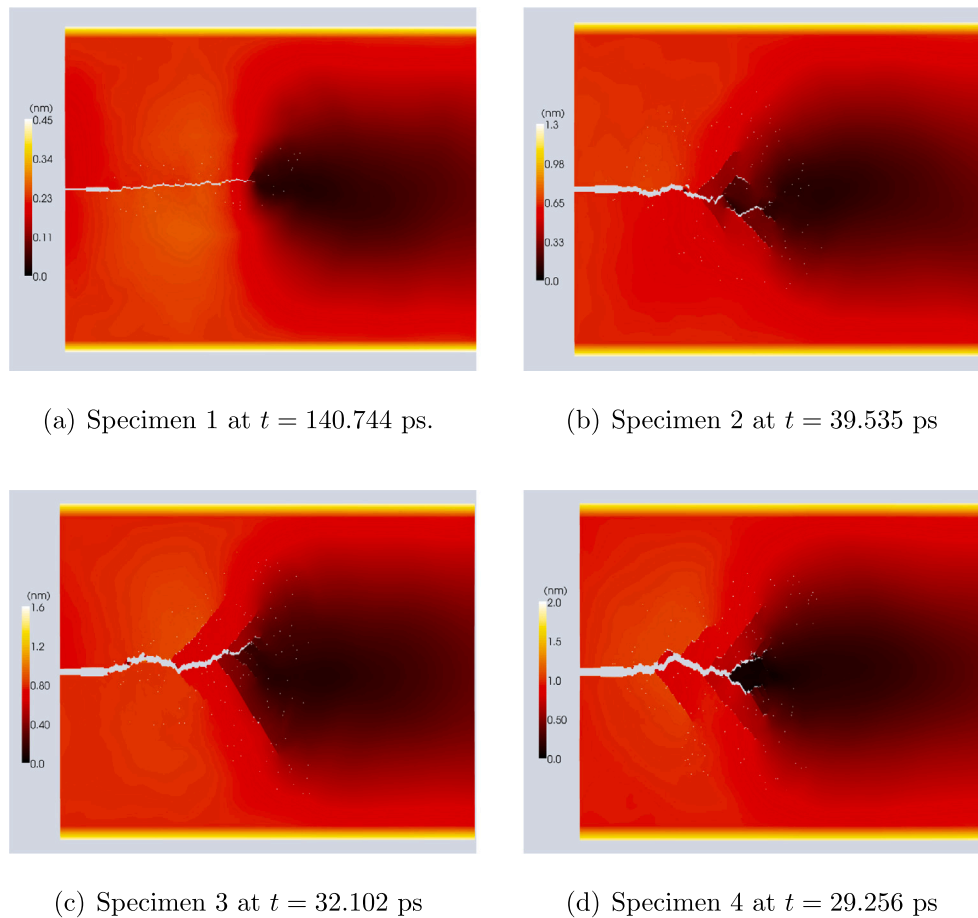
(a) Specimen 1 at $t = 140.744$ ps.

(b) Specimen 2 at $t = 39.535$ ps

(c) Specimen 3 at $t = 32.102$ ps

(d) Specimen 4 at $t = 29.256$ ps

Fig. 2. Cracked specimens at the end of the simulations.

2.4. Example simulation of dynamic fracture

As an example we consider a copper single crystal in the (111) plane, so that the two-dimensional lattice is hexagonal. A Lennard-Jones potential is used with the parameter set [30]: $a = 0.415$ eV and $b = 0.2277$ nm. The Young's modulus E and Poisson's ratio v for the continuum then become: $E = 79.334$ GPa and $v = 0.25$. The copper atomic mass is taken as $m = 0.1055 \times 10^{-24}$ kg, which corresponds to a mass density $\rho = 1865.25 \times 10^3$ kgm^{-3}. In the present study, the temperature has not been taken into account. To include the temperature a 'thermal equilibrium' has to be achieved in addition to the mechanical equilibrium, for instance using the Nose–Hoover thermostat method [31].

The domain of interest is 100 nm long and 77.5 nm wide with an initial crack. A large MD-Box is considered in order to properly trace the crack propagation. The finite element mesh consists of 1221 quadrilateral elements and 4868 nodes, and the initial notch has been applied using the extended finite element technique, see Section 4. The element size is about 10 times the inter-atomic distance. 8875 atoms are put in the initial MD-Box. The width of the coupling domain is approximately 3 nm and 33% of the atoms in this region hold Lagrange multipliers. For computational reasons, the results have been obtained by only including the first neighbours in the atomistic interactions, since the equilibrium-finding and updating are expensive operations when including many neighbours. However, simulations on a smaller scale suggest that, at least qualitatively, the results are similar. In order to simulate defects in the lattice, 0.5% of the atoms are removed in a random manner.

Example calculations have been carried out for four loading rates, applied to the top and bottom edges of the specimen: $V_p = 3.16$ ms^{-1},

$V_p = 31.6$ ms^{-1}, $V_p = 47.4$ ms^{-1}, $V_p = 63.2$ ms^{-1} and $V_p = 126.5$ ms^{-1}. From Fig. 2 we observe that for the lowest loading rate there is a single main crack, which propagates in a rather straight manner. For the two next higher loading rates secondary branches develop, while for the highest loading rate crack branching occurs and the main crack shows a tortuous pattern.

3. Fracture mechanics

The seminal papers of [1,2] mark the start of the development of Linear Elastic Fracture Mechanics (LEFM) as a branch of engineering mechanics which has contributed much to the understanding of the propagation of initial flaws in structures. The solution of displacements and stresses around elliptical holes in elastic bodies [1] was the basis for the observation [2] that, for the limiting case that the elliptical hole reduces to a crack, the stresses at the crack tip become singular. Indeed, in LEFM the stresses at a sharp crack tip are singular, and the traditional strength criterion, where the maximum stress is compared with the tensile strength of the material, say f_t, no longer suffices to assess whether crack propagation will occur or not. Instead, the critical energy release rate $\mathcal{G}_c$, also named the fracture energy in non-linear theories for fracture such as cohesive-zone models, plays a central role. This is the energy needed to create a unit area of crack.

The idea of Linear Elastic Fracture Mechanics is simple, and departs from considering an existing crack in an infinite plate which is composed of a linear elastic material and is subject to a far-field all-around stress σ_∞. The difference between the stored elastic energy in the plate and the surface energy at the crack surface subsequently plays a central role in the further development of the theory. A crucial outcome of
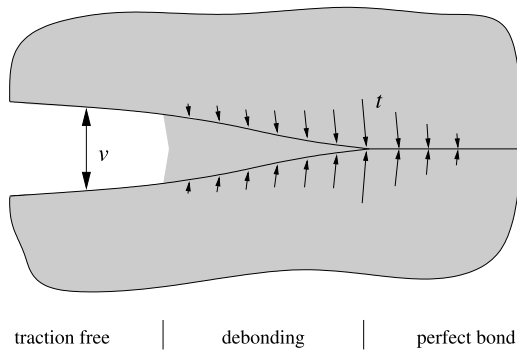
traction free | debonding | perfect bond

Fig. 3. Schematic representation of a cohesive zone.

the theory is that there is an internal length scale, commonly defined as [32–34]:

$$\ell = \frac{E\mathcal{G}_c}{f_t^2} \tag{7}$$

with E Young's modulus and f_t the tensile strength. It is emphasised that the presence of an internal length scale implies that there is a size effect in fracture mechanics, which is absent in a pure strength-based theory.

3.1. Cohesive fracture

An important issue when considering damage and fracture is the observation that most geomaterials are not perfectly brittle in the Griffith sense, but display a softening branch after reaching the strength limit. This softening behaviour is caused by their heterogeneous character, which promotes phenomena like micro-cracking, local crack branching, crack arrest by hard particles and void initiation in a *fracture process zone* ahead of the visibly observable crack tip. In concrete, this is exacerbated by the presence of reinforcement, by the exothermal processes that occur during maturing and hardening, and due to the shrinkage that occurs as a consequence of moisture diffusion and the subsequent water loss. These phenomena cannot be captured using classical fracture mechanics approaches. A further issue is that in LEFM crack propagation is assumed to be initiated from a pre-existing crack-like flaw.

Only if the fracture process zone is sufficiently small compared to the structural dimensions, i.e. if $\ell \ll \mathcal{L}$, with $\mathcal{L}$ a characteristic structural dimension, and if there exists an initial crack-like flaw, Linear-Elastic Fracture Mechanics concepts apply. However, if this is not the case, like in most geomaterials, but also in many biomaterials, the cohesive tractions in the fracture process zone must be taken into account. A most powerful and natural approach is the use of cohesive-zone models, which were introduced by Dugdale and [4] and Barenblatt [5] for elastic–plastic fracture in ductile metals, and for quasi-brittle materials by Hillerborg et al. [35] in their so-called Fictitious Crack Model. Different from Linear Elastic Fracture Mechanics, the cohesive surface methodology also permits the analysis of fracture processes in which there is no dominant flaw [35,36], even though in the original contributions [4,5] a dominant flaw was assumed to be present.

In cohesive-zone models, the degrading mechanisms in front of the actual crack tip are lumped into a discrete line (or a plane in three dimensions), see Fig. 3, and a relation between the tractions at the discontinuity $\mathbf{t}_d$ and the relative displacements $[\![\mathbf{u}]\!]$ across this line or plane represents the degrading mechanisms in the fracture process zone:

$$\mathbf{t}_d = \mathbf{t}_d([\![\mathbf{u}]\!], \kappa) \tag{8}$$

with κ an internal variable, which memorises the largest value of a (material-dependent) function of the relative displacements. Fig. 4 shows some commonly used decohesion relations, a simple linear relation (left), a relation often used for ductile fracture (centre) [37], and one typical of quasi-brittle fracture (right) [38]. For ductile fracture, the most important parameters of the cohesive-zone model appear to be the tensile strength f_t and the fracture energy or work of separation $\mathcal{G}_c$ [39], formally defined as:

$$\mathcal{G}_c = \int_{v_n=0}^{\infty} t_n \mathrm{d}v_n \tag{9}$$

with t_n and $v_n = [\![u_n]\!]$ the normal traction and the normal relative displacement across the fracture process zone. For more brittle decohesion relations as shown for instance in the right part of Fig. 4, i.e., when the decohesion law stems from micro-cracking as in concrete or ceramics, the shape of the stress–separation relation also plays a role and can be more important than the value of the tensile strength f_t [40].

From dimensional considerations, i.e. the presence of the fracture energy $\mathcal{G}_c$ and the Young's modulus E, one can conclude that a characteristic length ℓ is introduced in the model, similar to Linear Elastic Fracture Mechanics. Different from LEFM, however, no stress singularity exists.

Evidently, constitutive relations are specified independently for the bulk material and for one or more cohesive surfaces. The cohesive constitutive relation embodies the failure characteristics of the material and characterises the separation process. The bulk and cohesive constitutive relations together with appropriate balance laws and boundary (and initial) conditions completely specify the problem. Fracture is thus a natural outcome of the constitutive relations in the bulk and the interface, together with the balances of mass and momentum.

3.2. Distributing cohesive fracture

The cohesive-zone model is essentially a discrete concept, but it can be cast into a continuum format by distributing the fracture energy $\mathcal{G}_f$ over a finite thickness w [41,42]. We obtain:

$$\mathcal{G}_f = \int_{n=0}^{w} \int_{\epsilon_{nn}=0}^{\infty} \sigma_{nn} \mathrm{d}\epsilon_{nn}(n) \mathrm{d}n, \tag{10}$$

with n the coordinate normal to the localisation plane, and σ_{nn} and ϵ_{nn} the normal stress and normal strain in the n-direction. For linear elements the strains are constant over the width of an element w, so that $\mathcal{G}_f = wg_f$, with g_f the energy dissipated per unit volume of fully damaged material:

$$g_f = \int_{\epsilon_{nn}=0}^{\infty} \sigma_{nn} \mathrm{d}\epsilon_{nn}. \tag{11}$$

The length scale w introduced into the model is proportional to the element size and therefore has a numerical nature.

The load–displacement curves that are computed in this manner can become fairly insensitive to the discretisation for a sufficient level of refinement. However, this holds much less so for the direction of the lines of the discretisation. Indeed, cracks tend to propagate along the lines of the discretisation, thus deviating from the physical crack path. Moreover, when quadratic or higher-order finite elements are used, the numerically obtained crack band width no longer coincides with the element size. Various formulas have been proposed to estimate the numerical length scale, depending on the interpolation order of the polynomials, the spatial integration scheme and the expected angle between the crack and the grid lines [43–45].

4. Discrete crack models

Initially, the discrete crack model was implemented by letting the crack grow when the nodal force at the node ahead of the crack tip exceeds a tensile strength criterion. Subsequently, the node is split into two nodes and the tip of the crack is assumed to propagate to the next node. When the tensile strength criterion is violated at this node, it is split and the procedure is repeated, as sketched in Fig. 5 [6].
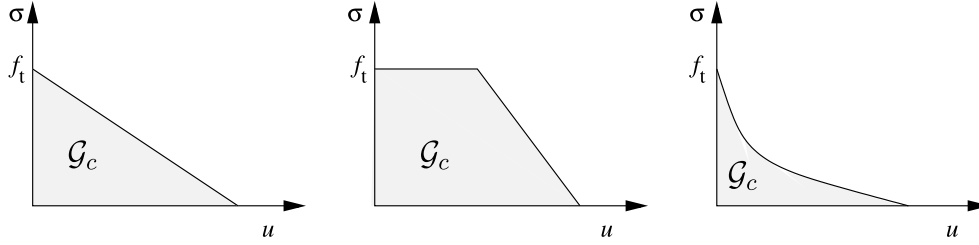
Fig. 4. Traction–displacement curves. Left: a linear relation. Centre: relation for a ductile solid. Right: relation for a quasi-brittle solid.
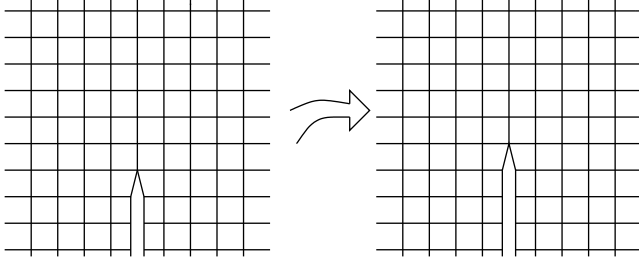

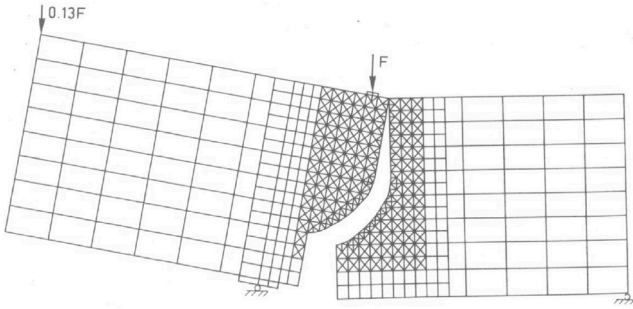**Fig. 5.** Earliest form of discrete crack modelling.

Fig. 6. Deformed configuration of a Single-Edge Notched beam that results from an analysis where interface elements equipped with a quasi-brittle cohesive-zone model have been placed a priori at the crack path known from experiments [46].

4.1. Remeshing

In the original format described above, the discrete crack approach has several disadvantages, the major issue being that cracks are forced to propagate along existing element boundaries, which predefines the crack path. Accordingly, a *mesh bias* is introduced. Automatic remeshing allows the mesh bias to be reduced, if not eliminated, and sophisticated computer codes with remeshing were developed by Ingraffea and co-workers [47]. While the initial remeshing algorithms exploited Linear Elastic Fracture Mechanics, algorithms that incorporate cohesive-zone models embedded in interface elements have also been developed [48–50].

4.2. The classic: Interface elements

If the crack path is known, either from experimental evidence, or because of the structure of the material (such as in laminated composites), the mesh can be adapted a priori to the expected lines or planes of crack propagation and interface elements can be inserted in the mesh at these locations. Under such circumstances interface elements equipped with cohesive-zone models have been used with considerable success as shown in Fig. 6 for mixed-mode fracture in a Single-Edge Notched concrete beam. In this example, the mesh has been designed such that the interface elements, which are equipped with a

quasi-brittle cohesive-zone model, are exactly located at the position of the experimentally observed crack path [46]. Another important application of the use of interface elements is delamination in composite materials. Since delamination initiation and propagation is restricted to the interfaces between plies, placing interface elements between the plies guarantees that the failure more will be captured exactly [52–55]. To allow for a more arbitrary direction of crack propagation it is also possible, as an alternative to remeshing, to insert interface elements between *all* continuum elements *a priori* [56]. Such an analysis can provide considerable insight in potential failure modes, but evidently suffers from a limited mesh bias. This has been demonstrated in [51], where the same Single-Edge Notched beam as in Fig. 6 was analysed, see Fig. 7.

The formulation of interface elements is relatively simple. The kinematic quantities in continuous interface elements are a set of mutually orthogonal, relative displacements: $[\![u_n]\!]$ for the opening mode, and $[\![u_s]\!]$, $[\![u_t]\!]$ for the two sliding modes. When collecting the relative displacements in a vector:

$$[\![\mathbf{u}]\!] = ([\![u_n]\!], [\![u_s]\!], [\![u_t]\!])^{\mathrm{T}} \tag{12}$$

which is defined in a local s, n, t-coordinate system, they can be related to the displacements $\mathbf{u}^+$ at the upper side of the interface, Γ_d^+, and the displacements $\mathbf{u}^-$ at the lower side of the interface, Γ_d^-, via

$$\mathbf{u}^+ - \mathbf{u}^- = \mathbf{R} [\![\mathbf{u}]\!] \tag{13}$$

where $\mathbf{u}^+, \mathbf{u}^-$ are expressed in the global x, y, z-coordinate system, and $\mathbf{R} = (\mathbf{n}_{\Gamma_d}, \mathbf{s}_{\Gamma_d}, \mathbf{t}_{\Gamma_d})$ is the standard rotation matrix between the local and the global coordinate system, with $\mathbf{s}_{\Gamma_d}, \mathbf{t}_{\Gamma_d}$ mutually orthogonal unit vectors aligned with the discontinuity, and $\mathbf{n}_{\Gamma_d}$ the unit vector normal to the discontinuity. The displacements are interpolated in a standard manner as:

$$\mathbf{u} = \mathbf{H}\mathbf{a}, \tag{14}$$

where

$$\mathbf{H} = \begin{bmatrix} \mathbf{h} & \mathbf{0} & \mathbf{0} \\ \mathbf{0} & \mathbf{h} & \mathbf{0} \\ \mathbf{0} & \mathbf{0} & \mathbf{h} \end{bmatrix} \tag{15}$$

and $\mathbf{a}$ is the nodal displacement array that contains the degrees of freedom related to the N nodes in case of a standard continuum element. For an interface element the nodes are doubled, one set of N nodes for the Γ_d^+ side of the interface, and another set of N nodes for the Γ^- side. The $1 \times N$ matrices contain the shape functions $h_1, \ldots, h_N$:

$$\mathbf{h} = (h_1 \ldots h_N) \tag{16}$$

The relation between the nodal displacements and the relative displacements for interface elements then reads:

$$[\![\mathbf{u}]\!] = \mathbf{R}(\mathbf{u}^+ - \mathbf{u}^-) = \mathbf{R}(\mathbf{H}\mathbf{a}^+ - \mathbf{H}\mathbf{a}^-) = \mathbf{R}\mathbf{B}\bar{\mathbf{a}} \tag{17}$$

with

$$\mathbf{B} = \begin{bmatrix} -\mathbf{h} & +\mathbf{h} & \mathbf{0} & \mathbf{0} & \mathbf{0} & \mathbf{0} \\ \mathbf{0} & \mathbf{0} & -\mathbf{h} & +\mathbf{h} & \mathbf{0} & \mathbf{0} \\ \mathbf{0} & \mathbf{0} & \mathbf{0} & \mathbf{0} & -\mathbf{h} & +\mathbf{h} \end{bmatrix} \tag{18}$$
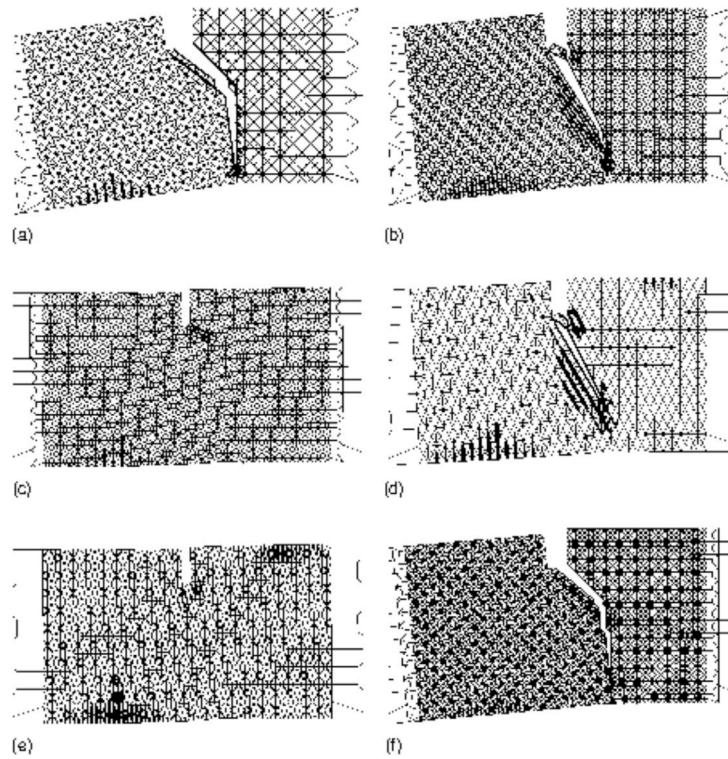
Fig. 7. Crack patterns for different discretisations using interface elements between *all* solid elements. Only the part of the Single Edge Notched beam near the notch is shown [51].
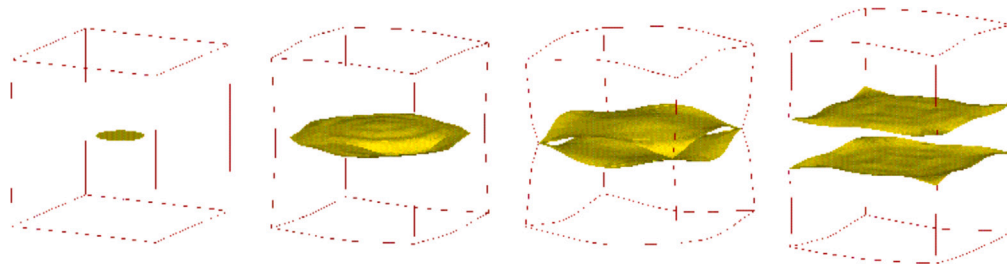
Fig. 8. Cube with an initial penny-shape crack: propagation of the crack towards the free surfaces of the specimen [57].

the relative displacement-nodal displacement matrix for the interface element, and $\bar{\mathbf{a}}$ containing the discrete nodal displacements at both sides of the interface expressed in the global x, y, z-coordinate system.

In the local coordinate system, the cohesive tractions $\mathbf{t}_d^{\mathrm{loc}}$ are related to the relative displacements $[\![\mathbf{u}]\!]$ via a nonlinear relation, cf Eq. (8):

$$\mathbf{t}_d^{\mathrm{loc}} = \mathbf{t}_d^{\mathrm{loc}} ([\![\mathbf{u}]\!], \kappa), \tag{19}$$

Similar to the relative displacements, the traction vector $\mathbf{t}_d^{\mathrm{loc}}$ can be related to the tractions in the global coordinate system using the rotation matrix $\mathbf{R}$:

$$\mathbf{t}_d^{\mathrm{loc}} = \mathbf{R}\mathbf{t}_d \tag{20}$$

For use in a Newton–Raphson iterative procedure the constitutive relation can be linearised as:

$$d\mathbf{t}_d^{\mathrm{loc}} = \mathbf{D}_d \, d[\![\mathbf{u}]\!] \tag{21}$$

with 'd' denoting a small increment, and

$$\mathbf{D}_d = \frac{\partial \mathbf{t}_d^{\mathrm{loc}}}{\partial [\![\mathbf{u}]\!]} \tag{22}$$

The limiting case that $\mathbf{t}_d^{\mathrm{loc}} = \mathbf{0}$ obviously represents a traction-free crack.
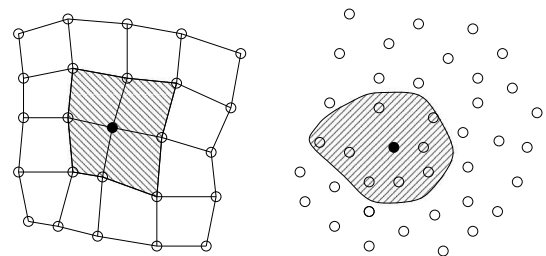
Fig. 9. Typical domain of influence in a numerical method with a nodal connectivity (left) and a meshless method (right). The domains of influence of the solid nodes are shaded.

4.3. Meshfree methods

In principle, the continuous change in topology inherent in the discrete crack approach can be handled easily by meshfree methods [58,59]. Indeed, successful analyses have been carried out using these methods, see for instance Fig. 8, which shows crack propagation in a cube with an initial penny-shaped crack [57].

We now take the Element-Free Galerkin (EFG) method as an example. Meshfree (or meshless) methods do not require an explicitly defined connectivity between nodes for the definition of the shape functions. Instead, each node has a domain of influence which does not depend on the arrangement of the nodes. The domain of influence of a node is the part of the domain over which the shape function of that specific node is non-zero. In finite element methods the domain of influence is set by node connections, whereas in a meshfree method the domain of influence can have a fairly arbitrary shape. Fig. 9 shows the domains of influence of nodes for a (finite element) method that requires a nodal connectivity (left) and for a meshless method (right).

In the Element-Free Galerkin method shape functions are formulated by applying a moving least squares approximation [60]. This approximation interpolates the nodal data, for example u_k, at a point $\mathbf{x}$ by

$$u(\mathbf{x}) = \mathbf{p}^{\mathrm{T}}(\mathbf{x})\mathbf{a}(\mathbf{x}) \tag{23}$$

where $\mathbf{p}(\mathbf{x})$ is a vector of basis functions (typically monomials) and $\mathbf{a}(\mathbf{x})$ is a vector of coordinate-dependent coefficients. In a moving least squares interpolation each node k in the domain of influence of the point $\mathbf{x}$ is assigned a weight function w_k, which renders the coefficients non-uniform. These weight functions appear in the L^2-norm as:

$$J_{\mathrm{mls}} = \sum_{k=1}^{n} w_k(\mathbf{x}) \left(\mathbf{p}^{\mathrm{T}}(\mathbf{x}_k)\mathbf{a}(\mathbf{x}) - u_k \right)^2 \tag{24}$$

A typical choice for the weight function is a Gaussian distribution, so that the weight function on the domain of influence – where it is positive – is bell-shaped. Elaboration of the stationarity requirement of J_{mls} with respect to the coefficients $\mathbf{a}(\mathbf{x})$ gives:

$$\mathbf{a}(\mathbf{x}) = \mathbf{A}_1^{-1}(\mathbf{x})\mathbf{A}_2(\mathbf{x})\mathbf{u} \tag{25}$$

where $\mathbf{u} = [u_1, u_2, \ldots, u_n]^T$ and

$$\mathbf{A}_1(\mathbf{x}) = \sum_{k=1}^{n} w_k(\mathbf{x})\mathbf{p}(\mathbf{x}_k)\mathbf{p}^{\mathrm{T}}(\mathbf{x}_k) \tag{26a}$$

$$\mathbf{A}_2(\mathbf{x}) = \left[w_1(\mathbf{x})\mathbf{p}(\mathbf{x}_1), w_2(\mathbf{x})\mathbf{p}(\mathbf{x}_2), \ldots, w_n(\mathbf{x})\mathbf{p}(\mathbf{x}_n) \right] \tag{26b}$$

Substitution of Eq. (25) into Eq. (23) then leads to

$$u(\mathbf{x}) = \underbrace{\mathbf{p}^{\mathrm{T}}(\mathbf{x})\mathbf{A}_1^{-1}(\mathbf{x})\mathbf{A}_2(\mathbf{x})}_{\mathbf{N}(\mathbf{x})} \mathbf{u} \tag{27}$$

and the matrix $\mathbf{N}(\mathbf{x})$ that contains the shape functions can be identified as:

$$\mathbf{N}(\mathbf{x}) = \mathbf{p}^{\mathrm{T}}(\mathbf{x})\mathbf{A}_1^{-1}(\mathbf{x})\mathbf{A}_2(\mathbf{x}) \tag{28}$$

Shape functions which are generated in this manner are usually not of a polynomial form, even though $\mathbf{p}(\mathbf{x})$ contains only polynomial terms. When moving least squares shape functions are used, the weight functions that are attached to each node determine the degree of continuity of the interpolants and the extent of the support of the node. A high degree of continuity can thus be achieved. The support of one node normally includes several other nodes and is therefore less compact than with finite element methods, and leads to a larger band width of the system of equations. In contrast to finite element methods, the shape functions that arise in the Element-Free Galerkin approach are not interpolating, and the nodal parameters u_k contained in the array $\mathbf{u}$ in Eq. (25) are not the nodal values of the approximant function $u(\mathbf{x})$. The absence of interpolatibility can complicate the imposition of essential boundary conditions and constraint equations.

Discontinuous shape functions can be obtained in a straightforward manner by truncating the appropriate weight functions. Special attention needs to be paid to the weight function in the vicinity of a crack tip in order to adequately represent the continuity of the displacement field. Fig. 10 illustrates three different procedures how to truncate the domain of influence in the case of intersection by a crack [61].

Besides this straightforward manner of introducing discontinuous shape functions, the Element-Free Galerkin method facilitates the enrichment of the solution space, for instance when capturing stress singularities at crack tips which occur in Linear Elastic Fracture Mechanics. This is achieved by locally enriching the base vector $\mathbf{p}(\mathbf{x})$ with singular tip functions [61].

Although meshfree methods were initially thought to provide an elegant framework for the mesh-independent simulation of fracture propagation, they appear to be less robust than finite element methods. They are computationally more demanding and the implementation in three dimensions appears to be less straightforward. Also, the manner in which the support of a node is changed in the presence of a crack is somewhat ad-hoc [62] and there is the need to employ a background 'mesh' of integration cells in most meshfree methods. These complications have limited the use of these methods.

4.4. The EXtended Finite Element Method

The eXtended Finite Element Method (XFEM) [63,64], can be viewed as a generalisation of interface elements which can be put arbitrarily within elements. This is enabled by the partition-of-unity property of finite element shape functions [65]. Also, the name generalised finite element method (GFEM) has been coined [66]. A collection of functions h_k, associated with node k, form a partition of unity if

$$\sum_{k=1}^{n} h_k(\mathbf{x}) = 1 \tag{29}$$

with n the number of discrete nodal points. For a set of shape functions h_k that satisfy the partition-of-unity property, a field u can be interpolated as follows:

$$u(\mathbf{x}) = \sum_{k=1}^{n} h_k(\mathbf{x}) \left(\bar{a}_k + \sum_{l=1}^{m} \psi_l(\mathbf{x})\hat{a}_{kl} \right) \tag{30}$$

with $\bar{a}_k$ the 'regular' nodal degrees of freedom, $\psi_l(\mathbf{x})$ the enhanced basis terms, and $\hat{a}_{kl}$ the additional degrees of freedom at node k, which represent the amplitudes of the lth enhanced basis term $\psi_l(\mathbf{x})$. A basic requirement of the enhanced basis terms ψ_l is that they are linearly independent, mutually, but also with respect to the original set of functions h_k. In standard finite element notation we can write the interpolation of a displacement field $\mathbf{u}$ as:

$$\mathbf{u} = \mathbf{H}(\bar{\mathbf{a}} + \boldsymbol{\Psi}\hat{\mathbf{a}}) \tag{31}$$

where $\mathbf{H}$ contains the standard shape functions and $\boldsymbol{\Psi}$ the enhanced basis terms. The arrays $\bar{\mathbf{a}}$ and $\hat{\mathbf{a}}$ collect the standard and the additional nodal degrees of freedom, respectively.

The enhanced basis terms can be exploited to model a discontinuity. Indeed, a displacement field that contains a single discontinuity can be represented by choosing [63,64,67,68]:

$$\boldsymbol{\Psi} = \mathcal{H}_{\Gamma_d}\mathbf{I} \tag{32}$$

with $\mathcal{H}_{\Gamma_d}$ the Heaviside function, which separates the Ω^--domain from the Ω^+-domain, Fig. 11. Substitution into Eq. (31) gives:

$$\mathbf{u} = \underbrace{\mathbf{H}\bar{\mathbf{a}}}_{\bar{\mathbf{u}}} + \mathcal{H}_{\Gamma_d}\underbrace{\mathbf{H}\hat{\mathbf{a}}}_{\hat{\mathbf{u}}} \tag{33}$$

Identifying the continuous fields $\bar{\mathbf{u}} = \mathbf{H}\bar{\mathbf{a}}$ and $\hat{\mathbf{u}} = \mathbf{H}\hat{\mathbf{a}}$ we observe that Eq. (33) exactly describes a displacement field that is crossed by a single discontinuity, but is otherwise continuous. Accordingly, the partition-of-unity property of finite element shape functions can be used in a straightforward manner to incorporate discontinuities in a continuum such that their discontinuous character is fully preserved.

To derive the discrete format of the extended finite element method, we take the balance of momentum as point of departure. First, we restrict the derivation to quasi-static loading conditions and neglect body forces for simplicity. This gives:

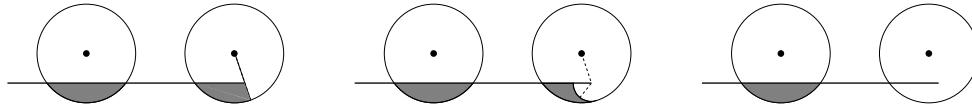$$\nabla \cdot \boldsymbol{\sigma} = \mathbf{0} \tag{34}$$

Fig. 10. Domains of influence intersected by a crack or the crack tip: truncation of the weight function according to the visibility criterion (left), the diffraction criterion (centre) and the see-through criterion (right) – the shaded areas denote the neglected part of the domain of influence.
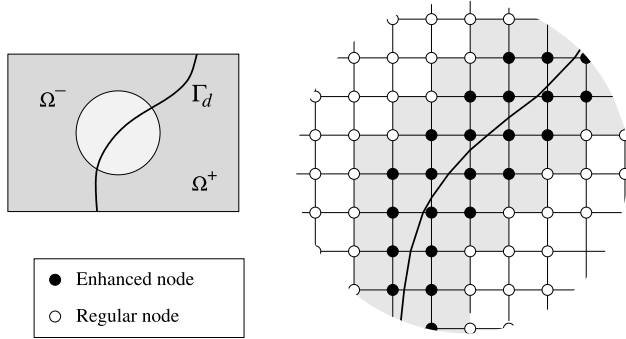

Fig. 11. Two-dimensional finite element mesh with a discontinuity denoted by the bold line. The grey elements contain additional terms in the internal force vector and in the stiffness matrix.

We multiply this identity by test functions $\boldsymbol{\eta}$, and in a Bubnov–Galerkin sense, take them from the same space as the trial functions for **u**. For elements that are crossed by a discontinuity, the test functions are taken as:

$$\boldsymbol{\eta} = \bar{\boldsymbol{\eta}} + \mathcal{H}_{\Gamma_d}\hat{\boldsymbol{\eta}} \tag{35}$$

and a similar expression holds for the trial functions. Applying the divergence theorem and requiring that this identity holds for arbitrary $\bar{\boldsymbol{\eta}}$ and $\hat{\boldsymbol{\eta}}$ yields the following set of coupled equations:

$$\int_{\Omega} \nabla\bar{\boldsymbol{\eta}} : \boldsymbol{\sigma}\,\mathrm{d}\Omega = \int_{\Gamma} \bar{\boldsymbol{\eta}} \cdot \mathbf{t}_p\,\mathrm{d}\Gamma \tag{36a}$$

$$\int_{\Omega^+} \nabla\hat{\boldsymbol{\eta}} : \boldsymbol{\sigma}\,\mathrm{d}\Omega + \int_{\Gamma_d} \hat{\boldsymbol{\eta}} \cdot \mathbf{t}_d\,\mathrm{d}\Gamma = \int_{\Gamma} \mathcal{H}_{\Gamma_d}\hat{\boldsymbol{\eta}} \cdot \mathbf{t}_p\,\mathrm{d}\Gamma \tag{36b}$$

where in the volume integrals the Heaviside function has been eliminated by a change of the integration domain from Ω to Ω^+. Interpolating the trial and the test functions in the same space,

$$\begin{cases} \bar{\mathbf{u}} = \mathbf{H}\bar{\mathbf{a}} \quad , \quad \hat{\mathbf{u}} = \mathbf{H}\hat{\mathbf{a}} \\ \\ \bar{\mathbf{w}} = \mathbf{H}\bar{\boldsymbol{\eta}} \quad , \quad \hat{\mathbf{w}} = \mathbf{H}\hat{\boldsymbol{\eta}} \end{cases} \tag{37}$$

and requiring that the resulting equations must hold for any admissible $\bar{\mathbf{w}}$ and $\hat{\mathbf{w}}$, we obtain the discrete format:

$$\begin{aligned} \mathbf{f}_{\bar{u}}^{\text{ext}} &= \mathbf{f}_{\bar{u}}^{\text{int}} \\ \mathbf{f}_{\hat{u}}^{\text{ext}} &= \mathbf{f}_{\hat{u}}^{\text{int}} \end{aligned} \tag{38}$$

with the external force vectors,

$$\begin{aligned} \mathbf{f}_{\bar{u}}^{\text{ext}} &= \int_{\Gamma} \mathbf{H}^{\text{T}}\mathbf{t}_p\,\mathrm{d}\Gamma \\ \mathbf{f}_{\hat{u}}^{\text{ext}} &= \int_{\Gamma} \mathcal{H}_{\Gamma_d}\mathbf{H}^{\text{T}}\mathbf{t}_p\,\mathrm{d}\Gamma \end{aligned} \tag{39}$$

and the internal force vectors defined as:

$$\begin{aligned} \mathbf{f}_{\bar{u}}^{\text{int}} &= \int_{\Omega} \mathbf{B}_u^{\text{T}}\boldsymbol{\sigma}\,\mathrm{d}\Omega \\ \mathbf{f}_{\hat{u}}^{\text{int}} &= \int_{\Omega^+} \mathbf{B}_u^{\text{T}}\boldsymbol{\sigma}\,\mathrm{d}\Omega + \int_{\Gamma_d} \mathbf{H}^{\text{T}}\mathbf{t}_d\,\mathrm{d}\Gamma \end{aligned} \tag{40}$$

and standard strain-nodal displacement matrix $\mathbf{B}_u$. Linearisation then yields the following matrix–vector equation:

$$\begin{bmatrix} \mathbf{K}_{\bar{u}\bar{u}}^{\Omega} & \mathbf{K}_{\bar{u}\hat{u}}^{\Omega} \\ \mathbf{K}_{\hat{u}\bar{u}}^{\Omega} & \mathbf{K}_{\hat{u}\hat{u}}^{\Omega} + \mathbf{K}_{\hat{u}\hat{u}}^{\Gamma_d} \end{bmatrix} \begin{pmatrix} \mathrm{d}\bar{\mathbf{a}} \\ \mathrm{d}\hat{\mathbf{a}} \end{pmatrix} = \begin{pmatrix} \mathbf{f}_{\bar{u}}^{\text{ext}} \\ \mathbf{f}_{\hat{u}}^{\text{ext}} \end{pmatrix} - \begin{pmatrix} \mathbf{f}_{\bar{u}}^{\text{int}} \\ \mathbf{f}_{\hat{u}}^{\text{int}} \end{pmatrix} \tag{41}$$

with the submatrices given by:

$$\begin{aligned} \mathbf{K}_{\bar{u}\bar{u}}^{\Omega} &= \int_{\Omega} \mathbf{B}_u^{\text{T}}\mathbf{D}\mathbf{B}_u\,\mathrm{d}\Omega \\ \mathbf{K}_{\bar{u}\hat{u}}^{\Omega} &= \mathbf{K}_{\hat{u}\bar{u}}^{\Omega} = \mathbf{K}_{\hat{u}\hat{u}}^{\Omega} = \int_{\Omega^+} \mathbf{B}_u^{\text{T}}\mathbf{D}\mathbf{B}_u\,\mathrm{d}\Omega \\ \mathbf{K}_{\hat{u}\hat{u}}^{\Gamma_d} &= \int_{\Gamma_d} \mathbf{H}^{\text{T}}\mathbf{D}_d\mathbf{H}\,\mathrm{d}\Gamma \end{aligned} \tag{42}$$

If the material tangential stiffness matrices of the bulk and of the interface, $\mathbf{D}$ and $\mathbf{D}_d$, respectively, remain symmetric, symmetry is preserved for the full tangential stiffness matrix. It is noted that the additional degrees of freedom are not condensed at element level, but are included in the force vector and stiffness matrix in order to properly represent the discontinuity across inter-element boundaries.

The introduction of enhanced basis terms normally deteriorates the condition of the stiffness matrix. In particular when the discontinuity crosses an element in the vicinity of a node the contributions of the various terms in the stiffness matrix will have different magnitudes, which can lead to a stiffness matrix that is ill-conditioned. This problem can be ameliorated by only enhancing a node when it has a significant contribution to the stiffness matrix. Therefore, when the discontinuity splits an element such that a part of the element is much smaller than the other part, the node that supports the smallest part is not enhanced if [67]:

$$\frac{\min(\Omega^+, \Omega^-)}{\Omega} < \varepsilon \tag{43}$$

with ε a tolerance. Evidently, this will affect the computational results, but for reasonable values of ε, e.g. $\varepsilon \approx 0.05$, numerical experience shows that these effects are small [69].

The structured mesh of Fig. 11 is now used to further illustrate the concept. Nodes with a support that is crossed by a discontinuity are enhanced. These are marked by filled circles. The other nodes, denoted by the open circles, remain unchanged. Since only the nodes of elements that are crossed by the discontinuity have additional degrees of freedom, the increase in the total number of degrees of freedom is limited compared to the case without a discontinuity. When an element is supported by one or more enhanced nodes, additional terms will emerge in the internal force vector and in the stiffness matrix.

Another possibility is to use the enhanced basis terms to represent singularities, for instance the $\sqrt{r}$ near-tip displacement field that ensues in linear-elastic fracture mechanics. The enrichment functions that have to be added to the polynomial displacement field are:

$$\begin{aligned} \psi_1 &= \sqrt{r}\cos(\theta/2) \\ \psi_2 &= \sqrt{r}\sin(\theta/2) \\ \psi_3 &= \sqrt{r}\sin(\theta/2)\sin(\theta) \\ \psi_4 &= \sqrt{r}\cos(\theta/2)\sin(\theta) \end{aligned} \tag{44}$$

Clearly, these functions are linearly independent from polynomial basis functions. Also, they are mutually linearly independent, since they have been derived on this premise.

Since a key point of the extended finite element method is that the enrichment is local, enhanced basis functions that accommodate a
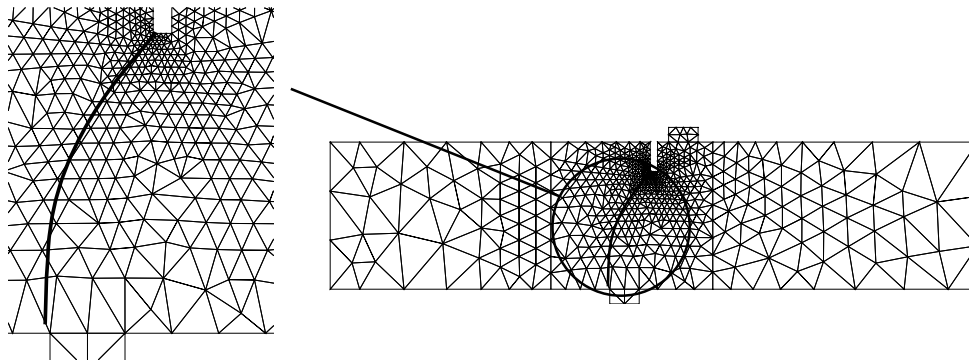
Fig. 12. Crack path that results from the analysis of the single-edge notched beam [67].
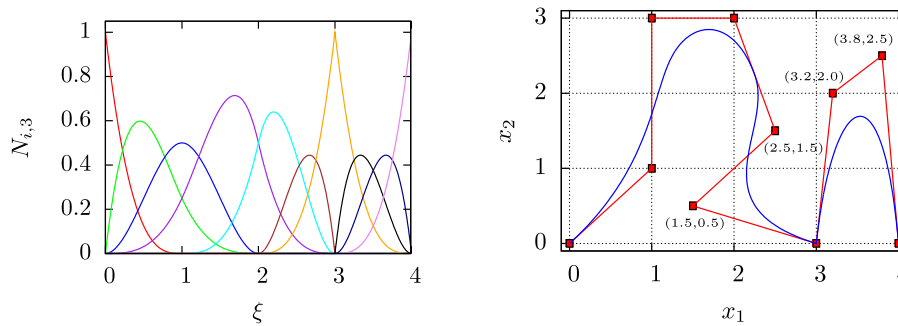

Fig. 13. (Left) Third-order B-spline basis functions constructed over the knot vector $\Xi = \{0,0,0,0,1,2,2,3,3,3,4,4,4,4\}$. (Right) Open B-spline curve (in blue) constructed using the control net shown in red.

stress singularity, like those stemming from Eq. (44), can be combined with those that represent a discontinuity, as in Eq. (32), in a single analysis. This is useful, for instance, when carrying out crack propagation analyses that are based on linear elastic fracture mechanics. In that case, additional basis function like in Eq. (44) are added around the crack tip, while Heaviside functions as in Eq. (32) are added in the wake of the tip.

An example of the application of the eXtended Finite Element method is given in Fig. 12 for the Single-Edge Notched Beam (SEN beam) of Fig. 6 as the numerically computed crack path of Fig. 12 is in excellent agreement with experimental observations. It is noted that the excellent agreement also depends on the smoothness of the stress field. Normally, the stresses are non-smooth around a crack tip, but a stress averaging over a finite domain, typically with a radius of three to four elements, results in stresses that can reliably be used in the crack propagation criterion [67].

4.5. Isogeometric finite element analysis

The fundamental idea of isogeometric analysis [70] is to directly use geometric design models for analysis purposes, thereby by-passing the need for meshing operations. Originally, Non-Uniform Rational B-Splines (NURBS) have been used, but more recently T-splines [71] have also been used to overcome some of the deficiencies of NURBS. Perhaps bigger advantages of splines are the smoothness of the interpolation, and the ease to elevate and reduce the order of interpolation, e.g. from C^0 to C^1 and vice versa.

A univariate B-spline is a parameterised curve which maps the one dimensional parameter domain $\hat{\Omega}$ onto a curve in the physical domain Ω through, see Fig. 13:

$$\mathbf{x}(\xi) = \sum_{k=1}^{n} N_{k,p}(\xi)\mathbf{X}_k \tag{45}$$

In this expression $\{N_{k,p}(\xi)\}_{k=1}^{n}$ are piecewise polynomial shape functions, with n and p denoting the number and order of basis functions,

respectively. The coefficients $\mathbf{X}_k$ – which play a similar role as the nodal coordinates in the finite element method – are referred to as the control points. The basis functions are defined over a non-decreasing knot vector $\Xi = \{\xi_1, \xi_2, \ldots, \xi_{n+p+1}\}$, which subdivides the parameter domain into elements (positive knot intervals). Here we will restrict the discussion to open B-splines, the class of B-splines which is created using knot vectors in which the first and the last knot values are repeated $p + 1$ times.

The B-spline basis $\{N_{k,p}(\xi)\}_{k=1}^{n}$ is defined recursively, starting with piecewise constant ($p = 0$) functions:

$$N_{i,0}(\xi) = \begin{cases} 1 & \xi_i \leq \xi < \xi_{i+1} \\ 0 & \text{otherwise} \end{cases} \tag{46}$$

from which the higher-order ($p = 1, 2, \ldots$) basis functions follow from the Cox-de Boor recursion formula [72,73]:

$$N_{i,p}(\xi) = \frac{\xi - \xi_i}{\xi_{i+p} - \xi_i} N_{i,p-1}(\xi) + \frac{\xi_{i+p+1} - \xi}{\xi_{i+p+1} - \xi_{i+1}} N_{i+1,p-1}(\xi) \tag{47}$$

The continuity of B-spline basis functions depends on the order of the B-spline and the multiplicity of the knots, see Fig. 13. When a knot is not repeated, a B-spline is C^{p-1}-continuous. At a knot with multiplicity m the continuity is equal to C^{p-m}. Hence, higher-order continuous bases can be constructed directly by increasing the B-spline order. As for C^0-continuous Lagrange finite elements, univariate B-spline elements support $p + 1$ basis functions. This implies that the band width of the constructed matrices is similar to that of higher-order C^0-continuous finite elements. Since B-spline basis functions are non-interpolatory, the imposition of essential boundary conditions directly through the control point coefficients is generally not possible, similar to meshfree methods. While simple boundary conditions such as constant edge displacements can be imposed directly, alternative methods, must be used for the imposition of more general essential boundary conditions.

A drawback of B-splines is their inability to exactly represent a number of objects that are of engineering interest, for instance, conic sections. For this reason, Non-Uniform Rational B-Splines (NURBS),

a rational generalisation of B-splines, have superseded B-splines in computer-aided geometric design. NURBS parameterise geometric objects with as basis functions:

$$r_k(\xi) = \frac{h_k(\xi) W_k}{w(\xi)} \tag{48}$$

where $w(\xi) = \sum_{k=1}^{N} h_k(\xi) W_k$ is the weighting function. Defining a NURBS requires the control net $\{\mathbf{p}_k\}_{k=1}^{N}$ to be supplemented with a set of scalar control point weights, $\{W_k\}_{k=1}^{N}$. Singularities in the rational basis functions are avoided by requiring all control point weights to be positive.

Multivariate B-splines, necessary for representing two and three-dimensional objects, are created by means of a tensor product structure. Surfaces and volumes constructed in this way are referred to as bivariate and trivariate patches, respectively. The required bivariate basis functions defined over the parameter domain $\widehat{V} \subset \mathbb{R}^2$ with parametric coordinate $\boldsymbol{\xi} = (\xi, \eta)$ are given by:

$$h_a(\boldsymbol{\xi}) = h_k(\xi) h_l(\eta) \tag{49}$$

with $a = (l-1)N_2 + k$ and univariate B-spline basis functions $h_k(\xi)$ and $h_l(\eta)$ defined over the knot vectors Ξ_ξ and Ξ_η, respectively. Note that we distinguish the bivariate basis functions, $\{h_a(\boldsymbol{\xi})\}_{a=1}^{N}$, from the univariate functions $\{h_k(\xi)\}_{k=1}^{N_1}$ and $\{h_l(\eta)\}_{l=1}^{N_2}$, by means of its argument, which is a scalar in the latter case, and a vector in the former case. By extension, the trivariate basis functions defined over the parameter domain $\widehat{V} \subset \mathbb{R}^3$ with parametric coordinate $\boldsymbol{\xi} = (\xi, \eta, \zeta)$ are

$$h_a(\boldsymbol{\xi}) = h_k(\xi) h_l(\eta) h_m(\zeta) \tag{50}$$

with $a = (m-1)N_1 N_2 + (l-1)N_2 + k$, and univariate B-spline basis function $h_m(\zeta)$ defined over the knot vector Ξ_ζ.

The availability of a Bézier representation for splines is of pivotal importance for the efficient implementation of isogeometric analysis, as it provides a unified approach to spline technologies that is compatible with standard finite element technology. The idea behind the Bézier representation is that since B-spline basis functions are piecewise polynomials, it is possible to express the B-spline basis functions over an element as a linear combination of a canonical set of basis functions. The element matrices containing the coefficients of these linear combinations are referred to as the element extraction operators. These extraction operators lump all global information – such as the inter-element continuity conditions – onto the elements.

When the element extraction operators are available, the basis functions can be constructed from the canonical set of elements. This makes isogeometric analysis an element technology, suitable to integrate in existing finite element codes. All information required for carrying out an analysis is assembled in a Bézier mesh, which contains:

- The (global) control net, $\{\mathbf{X}_k\}_{k=1}^{n}$, supplemented with control point weights, $\{W_k\}_{k=1}^{n}$, in the case of NURBS.
- A set of Bézier elements, each supplemented with a list containing the global indices of the basis functions with support over the element (commonly referred to as the connectivity array), and an element extraction operator.

The Bézier mesh can be regarded as an extension of the mesh used in standard finite element analysis, in which the control point weights and Bézier extraction operators are generally omitted.

As alluded to in the beginning of this subsection, higher-order continuity is important in problems which are described by higher-order differential equations, such as Kirchhoff–Love plates [75], in problems where higher-order gradients in the constitutive relation play a role as in gradient-damage models (see Section 5), or when fluxes (and their continuity) are important, for instance fluid fluxes in poroelasticity [76]. The ability of NURBS and T-splines to elevate or lower the order of continuity in a straightforward manner is useful in discrete crack propagation analysis. Indeed, lowering the order of continuity to C^{-1} is tantamount to creating a crack [74]. An example is shown in Fig. 14, where T-splines are used to model crack propagation in the Single-Edge Notched beam of Fig. 6.

5. Smeared crack analyses

As discussed in the preceding, the difficulties that come with discrete crack models, in particular the non-trivial implementation aspects and the complications which ensue when attempting to extend a discrete formulation to three dimensions, have led to ongoing attempts to formulate a neat and well-defined smeared-crack formulation. Herein, we will first provide a historical setting of the smeared-crack approach before outlining more systematic approaches embedded within the damage mechanics concept [77]. The incorporation of damage evolution within a classical, rate-independent continuum model comes with a caveat, namely the loss of well-posedness of the initial value problem and the consequential mesh sensitivity beyond a certain level of damage. Indeed, the inclusion of higher-order spatio-temporal derivatives is necessary to restore this well-posedness. Especially gradient-dependent damage models have become very popular. Although not used frequently, higher-order gradient damage models (with gradients higher than two) require a higher degree of continuity than standard C^0-continuous finite elements can offer, and in this context the Element-Free Galerkin method [78] and isogeometric finite element analysis [79] have been exploited successfully. The most recent development is the phase-field approach to brittle fracture, which bears similarities to gradient damage models.

5.1. Early approaches: stress drop and stiffness reduction

In the classical smeared-crack approach, the nucleation of one or more cracks in the volume that is attributed to an integration point is translated into a deterioration of the current stiffness and strength at that integration point. A crack is initiated when the combination of stresses satisfies a certain criterion, e.g. the major principal stress exceeds the tensile strength f_t. At this integration point the elastic, isotropic stress–strain relation is then replaced by an orthotropic elasticity-type relation with the n, s-axes being axes of orthotropy; n is the direction normal to the crack and s is the direction tangential to the crack. Initially, the orthotropic relation was defined as [7]:

$$\begin{pmatrix} \sigma_{nn} \\ \sigma_{ss} \\ \sigma_{ns} \end{pmatrix} = \begin{bmatrix} 0 & 0 & 0 \\ 0 & E & 0 \\ 0 & 0 & 0 \end{bmatrix} \begin{pmatrix} \epsilon_{nn} \\ \epsilon_{ss} \\ \gamma_{ns} \end{pmatrix} \tag{51}$$

for a plane-stress situation. Eq. (51) shows that both the normal stiffness and the shear stiffness across the crack were set equal to zero upon cracking. Consequently, all effects of lateral contraction/expansion disappear.

With $\boldsymbol{\sigma}_{\text{ns}} = (\sigma_{nn}, \sigma_{ss}, \sigma_{ns})^{\text{T}}$ and $\boldsymbol{\epsilon}_{\text{ns}} = (\epsilon_{nn}, \epsilon_{ss}, \gamma_{ns})^{\text{T}}$ we can also write the orthotropic elastic stiffness relation in the n, s-coordinate system as:

$$\boldsymbol{\sigma}_{\text{ns}} = \mathbf{D}^{\text{s}} \boldsymbol{\epsilon}_{\text{ns}} \tag{52}$$

where the secant stiffness matrix $\mathbf{D}^{\text{s}}$ is defined as:

$$\mathbf{D}^{\text{s}} = \begin{bmatrix} 0 & 0 & 0 \\ 0 & E & 0 \\ 0 & 0 & 0 \end{bmatrix} \tag{53}$$

If we introduce ϕ as the angle from the x-axis to the s-axis we can relate the components of $\boldsymbol{\epsilon}_{\text{ns}}$ and $\boldsymbol{\sigma}_{\text{ns}}$ to those in the global x, y-coordinate system via standard transformation matrices $\mathbf{T}_\epsilon(\phi)$ and $\mathbf{T}_\sigma(\phi)$: $\boldsymbol{\epsilon}_{\text{ns}} = \mathbf{T}_\epsilon(\phi) \boldsymbol{\epsilon}_{\text{xy}}$ and $\boldsymbol{\sigma}_{\text{ns}} = \mathbf{T}_\sigma(\phi) \boldsymbol{\sigma}_{\text{xy}}$. The local secant stiffness relation (52) then transforms into a secant stiffness relation in the global x, y-coordinate system:

$$\boldsymbol{\sigma}_{\text{xy}} = \mathbf{T}_\sigma^{-1}(\phi) \mathbf{D}^{\text{s}} \mathbf{T}_\epsilon(\phi) \boldsymbol{\epsilon}_{\text{xy}} \tag{54}$$

When ϕ changes continuously, e.g. to keep the direction of the crack orthogonal to the direction of the major principal stress, the rotating smeared crack model is obtained [80]. The approach with ϕ fixed at crack initiation is known as the fixed smeared crack model.
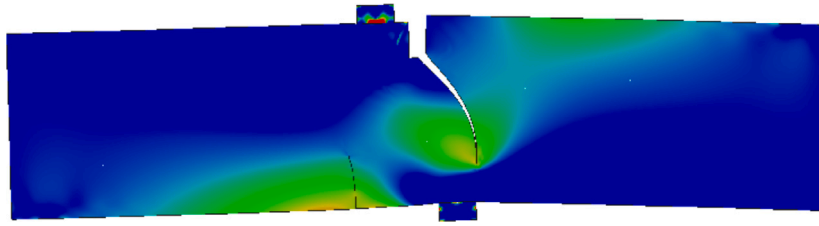
Fig. 14. Discrete crack analysis of Single-Edge Notched beam using T-splines [74].
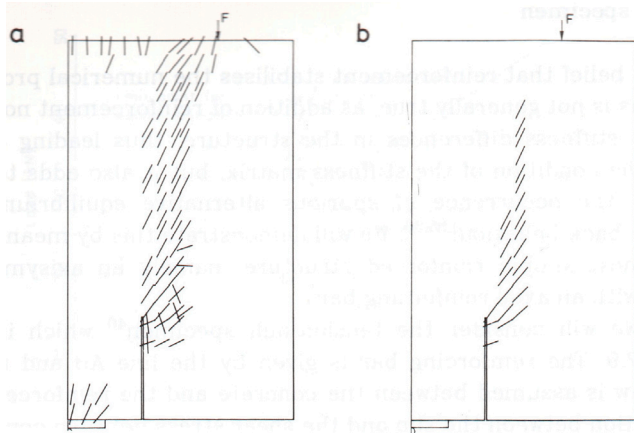

Fig. 15. Classical smeared-crack analysis. The central part of the Single-Edge Notched beam is shown. The short lines denote integration points where the tensile strength has been exceeded and are orthogonal to the major principal stress at the moment when it exceeded the tensile strength [82]. Subfigure (a) shows all smeared cracks, while subfigure (b) shows only those smeared cracks where no tensile stresses are transmitted.

Eq. (51) can lead to ill-conditioning of the tangential stiffness matrix and can lead to physically unrealistic and distorted crack pattern. To remedy these anomalies a reduced shear modulus $\beta G (0 \leq \beta \leq 1)$ was inserted in the stiffness relation [81], resulting in the following secant stiffness matrix:

$$\mathbf{D}^s = \begin{bmatrix} 0 & 0 & 0 \\ 0 & E & 0 \\ 0 & 0 & \beta G \end{bmatrix} \tag{55}$$

The use of the so-called shear retention factor β not only reduces numerical difficulties, but also improves the capturing the physics, because it can be regarded as a representation of some effects of friction or aggregate interlock within the crack.

Setting the stiffness normal to the crack in Eq. (55) equal to zero gives a sudden drop in stress from the tensile strength f_t to zero on crack initiation. Again, a sudden drop tends to cause numerical problems. A gradual decrease of the tensile carrying capacity, as in

$$\mathbf{D}^s = \begin{bmatrix} \mu E & 0 & 0 \\ 0 & E & 0 \\ 0 & 0 & \beta G \end{bmatrix} \tag{56}$$

gives results that are physically more appealing and computations that are numerically more stable. In Eq. (56), μ is a factor which gradually decreases from one to zero as a function of the normal strain ϵ_{nn}, $\mu = \mu(\epsilon_{nn})$. Further sophistication comes when the Poisson effect is restored partially.

The introduction of the reduced normal stiffness μE was originally motivated by the argument that in reinforced concrete the volume attributed to an integration point contains a number of cracks and that due to the bond between concrete and reinforcing steel, the intact concrete between the cracks adds stiffness which would be underestimated by a sudden drop to zero of the tensile strength (the so-called

tension-stiffening effect). Later, servo-controlled experiments on plain concrete have shown that concrete is not a perfectly brittle material in the Griffith sense, but that it has some residual load-carrying capacity after the tensile strength. Indeed, the term *quasi-brittle* has come en vogue for this class of materials, which encompasses concrete, rocks, ceramics, among others. The interpretation of the 'reduction' factor μ is now different, namely that it is related to the descending branch which models the gradually diminishing tensile strength of a quasi-brittle material upon further opening, often denoted as *tension-softening*.

An example of a smeared-crack analysis as outlined in the preceding is shown in Fig. 15, which depicts the centre part of the Single-Edge Notched beam analysed before using interface elements, cf. Fig. 6. Since the stresses are monitored in the integration points, the fracture criterion is evaluated in these points. Whenever the tensile strength is exceeded, a crack is formed and the isotropic stress–strain relation is replaced by Eq. (56). The crack is assumed to run orthogonal to the major principal stress at crack initiation and is visualised by a small line through the integration point in Fig. 15.

It is finally noted that finite element models with embedded discontinuities provide an elegant way to implement smeared-crack models [83–85]. Indeed, the embedded discontinuity approaches enhance the deformational capabilities of the elements, especially when the standard Bubnov–Galerkin approach is replaced by a Petrov–Galerkin method, which properly incorporates the discontinuity kinematics [86]. At the expense of a non-symmetric stiffness matrix, the high local strain gradients inside crack bands are captured more accurately. However, a true discontinuity is not obtained because the kinematics of the embedded crack band are diffused over the element when the governing equations are cast in a weak format. Indeed, for lower order elements it has been shown that the embedded discontinuity approaches and conventional smeared crack models are equivalent [87]. Consequently, the embedded discontinuity approaches inherit many of the disadvantages of conventional smeared crack models, including the sensitivity of crack propagation to the direction of mesh lines.

5.2. A proper framework: Damage mechanics

Starting from the late 1980s smeared-crack analysis has been carried out using the formalism of damage mechanics. Usually, an isotropic damage format has been used, which is why we will use this as a starting point. Formally, an isotropic format is not able to capture the smeared-crack approach outlined in the preceding subsection and an orthotropic version, which can be made equivalent with the classical smeared crack approaches has been developed [88]. Nevertheless, the differences in practical analyses are fairly small, which is why most analyses resort to the simpler isotropic format.

The basic stress–strain relation for an isotropic damage model reads:

$$\boldsymbol{\sigma} = (1 - \omega)\mathbf{D}^e : \boldsymbol{\epsilon} \tag{57}$$

with ω a scalar damage variable that grows from zero to one (at complete loss of integrity) and $\mathbf{D}^e$ the fourth-order elastic stiffness tensor. The total stress–strain relation, Eq. (57) is complemented by
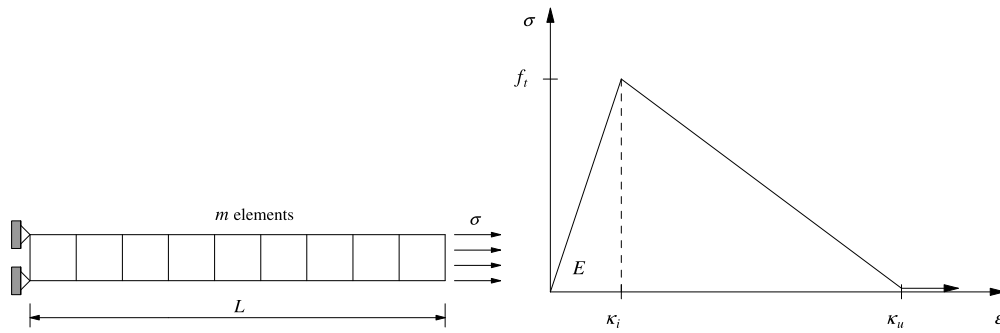
Fig. 16. Left: Bar with length L subject to an axial stress σ. Right: Elastic-linear damaging material behaviour.
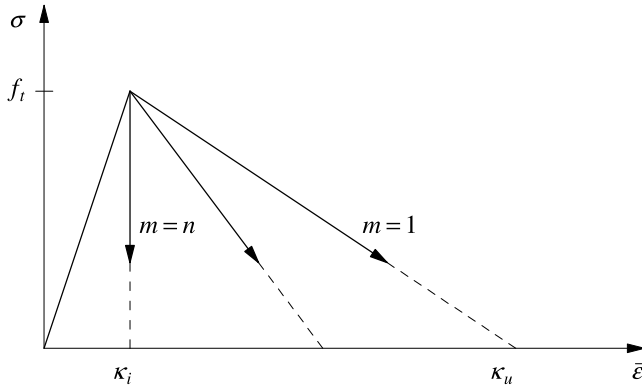

Fig. 17. Response of an imperfect bar in terms of a stress–average strain curve.

a damage-loading function f, which in a strain-based format reads as follows:

$$f = f(\tilde{\epsilon}, \kappa) \tag{58}$$

with $\tilde{\epsilon}$ a scalar-valued function of the strain tensor and κ the history variable. The damage-loading function f and the rate of the history variable, $\dot{\kappa}$, have to satisfy the Karush–Kuhn–Tucker loading–unloading conditions

$$f \leq 0, \quad \dot{\kappa} \geq 0, \quad \dot{\kappa} f = 0 \tag{59}$$

The history parameter κ starts at a damage threshold level κ_i and is updated by the requirement that during damage growth $f = 0$. Damage growth occurs according to an evolution law such that $\omega = \omega(\kappa)$, which can be determined from a uniaxial test.

For metals, a commonly accepted choice for $\tilde{\epsilon}$ is

$$\tilde{\epsilon} = \sqrt{\frac{1}{E}\, \epsilon : \mathbf{D}^e : \epsilon} \tag{60}$$

with E Young's modulus. However, this definition gives equal weights to tensile and compressive strain components, which makes it unsuitable to describe the mechanical behaviour of quasi-brittle materials like concrete and rock. To remedy this deficiency, [89] have suggested the definition

$$\tilde{\epsilon} = \sqrt{\sum_{i=1}^{3} \langle \epsilon_i \rangle^2} \tag{61}$$

with ϵ_i the principal strains, and $\langle \epsilon_i \rangle = \epsilon_i$ if $\epsilon_i > 0$ and $\langle \epsilon_i \rangle = 0$ otherwise. A third definition for the equivalent strain has been proposed in [90]. This proposition, for which the name Modified von Mises definition has been coined, is given by:

$$\tilde{\epsilon} = \frac{k-1}{2k(1-\nu)} I_1 + \frac{1}{2k}\sqrt{\frac{(k-1)^2}{(1-2\nu)^2}I_1^2 + \frac{6k}{(1+\nu)^2}J_2} \tag{62}$$

with I_1 the first invariant of the strain tensor and J_2 the second invariant of the deviatoric strain tensor. The parameter k governs the sensitivity to the compressive strain components relative to the tensile strain components. The definition of $\tilde{\epsilon}$ is such that a compressive uniaxial stress $k\sigma$ has the same effect as a uniaxial tensile stress σ. k is therefore normally set equal to the ratio of the compressive uniaxial strength and the tensile uniaxial strength.

5.3. Issues: Mesh dependence and poor convergence

A fundamental problem of incorporating damage evolution in standard continuum models is the inherent mesh sensitivity that occurs after reaching a certain damage level. This mesh sensitivity goes beyond the standard discretisation sensitivity of numerical approximation methods for partial differential equations and is not related to deficiencies in the discretisation method. Instead, the underlying reason for this mesh sensitivity is a local change in character of the governing partial differential equations. This local change of character of the governing set of partial differential equations leads to a loss of well-posedness of the initial boundary value problem and results in an infinite number of possible solutions. After discretisation, a finite number of solutions results. However, for a finer discretisation, the number of solutions increases, which explains the observed mesh sensitivity.

Mesh sensitivity in a standard continuum equipped with a strain-softening stress–strain relation is conveniently demonstrated by the example of a simple bar loaded in uniaxial tension. see Fig. 16. Let the bar be divided into m elements. Prior to reaching the tensile strength f_t, a linear relation is assumed between the normal stress σ and the normal strain ϵ: $\sigma = E\epsilon$. After reaching the peak strength, a descending slope is defined in this diagram through an affine transformation from the measured load–displacement curve. This is visualised in Fig. 16, where κ_u marks the point where the load-carrying capacity is exhausted. In the post-peak regime, the constitutive model thus reads:

$$\sigma = f_t + h(\epsilon - \kappa_i) \tag{63}$$

where, evidently, in case of degrading materials, $h < 0$ being the softening modulus. For linear softening, we have $h = -f_t/(\kappa_u - \kappa_i)$.

We next suppose that one element has a tensile strength that is marginally below that of the other $m - 1$ elements. Upon reaching the tensile strength of this element, failure will occur. In the other neighbouring elements, the tensile strength is not exceeded and they will unload elastically. Beyond the peak strength, the average strain in the bar is thus given by

$$\bar{\epsilon} = \frac{\sigma}{E} + \frac{E-h}{Eh}\frac{\sigma - f_t}{m} \tag{64}$$

For linear softening and introducing n as the ratio between the strain κ_u at which the residual load-carrying capacity is exhausted and the threshold damage level κ_i, $n = \kappa_u/\kappa_i$ and $h = -E/(n-1)$, gives

$$\bar{\epsilon} = \frac{\sigma}{E} + \frac{n(f_t - \sigma)}{mE} \tag{65}$$
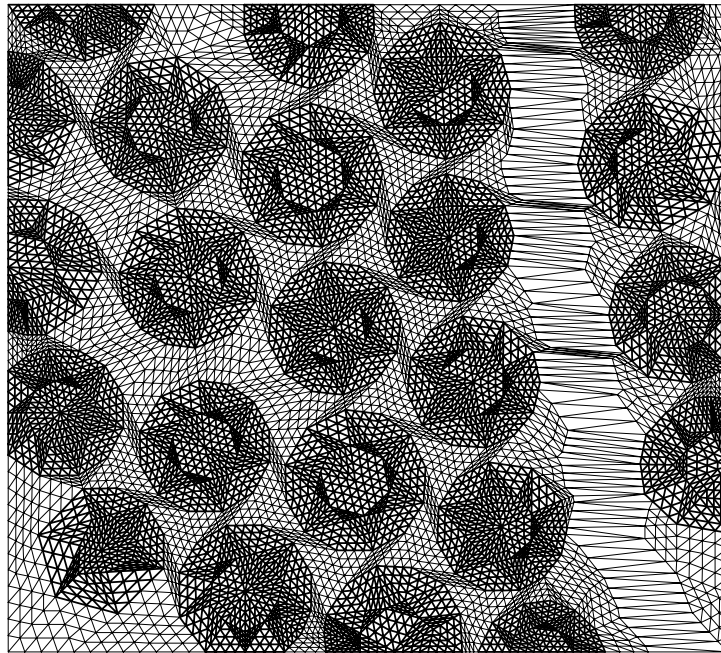
Fig. 18. Localised failure mode in a deformed SiC/C specimen [91].

This result has been plotted in Fig. 17 for different ratios of n/m. The computed post-peak curves do not seem to converge to a unique curve. In fact, they do, because the governing equations predict the failure mechanism to be a line crack with zero thickness. The numerical solution simply tries to capture this line crack, which results in a localisation in one element, irrespective of the width of the element. The impact on the stress–average strain curve is obvious: for an infinite number of elements ($m \rightarrow \infty$), the post-peak curve doubles back on the original loading curve. Indeed, the problem is that, since in continuum mechanics the constitutive model is phrased in terms of a *stress–strain* relation and not as a *force–displacement* relation, the energy that is dissipated tends to zero upon mesh refinement, simply because the volume in which the failure process occurs also becomes zero. From a physical point of view, this is unacceptable.

The above observations are by no means exclusive to the simple one-dimensional example discussed above. A more complicated boundary value problem is the silicium carbide specimen of Fig. 18 [91], which is reinforced with carbon fibres (SiC/C composite). The dimensions of the specimen are 30 μm×30 μm and a uniform horizontal loading is applied to the vertical sides. The fibres are assumed to remain elastic and also the bond between fibres and matrix material is assumed to be perfect. A degrading mechanism is only considered for the matrix material, for which a simple von Mises plasticity model with linear softening has been used.

After the onset of softening, a clear localisation zone develops, as is shown in Fig. 18. This figure shows the fine mesh, which consists of 15 568 elements. The computed load–displacement curve has been plotted in Fig. 19, together with those for the two coarser discretisations, with 3892 and 973 elements, respectively. The same picture arises as for the simple one-dimensional example: a more brittle behaviour is obtained when the mesh is refined and there seems to be convergence towards a solution with zero energy dissipation. In fact, the solution not only becomes more brittle upon mesh refinement, but also the peak load is reduced. Moreover, the solution process becomes very unstable for finer discretisations. This shows through the rather irregular shape of the load–displacement curve for the finest discretisation and by the observation that the solution could not be continued at some stage, no matter how sophisticated solution techniques were employed. The explanation for this phenomenon is that, as shown in the simple

bar problem, a refinement of the discretisation introduces more and more possible equilibrium states. The iterative solution process has to 'choose' between these equilibrium states and tends to pick another equilibrium state every subsequent iteration. Ultimately, this leads to a divergence of the iterative solution procedure.

From a mathematical perspective the severe mesh sensitivity is caused by the local loss of ellipticity, or, equivalently, loss of hyperbolicity for dynamic loadings. Since the underlying reason is of a mathematical rather than of a numerical nature, the sensitivity to the discretisation occurs for *any* discretisation method, including mesh-free methods [92].

5.4. Gradient-dependent damage models

In a non-local generalisation the equivalent strain $\tilde{\epsilon}$ is normally replaced by a spatially averaged quantity in the damage-loading function [93]:

$$f(\bar{\epsilon}, \kappa) = \bar{\epsilon} - \kappa \tag{66}$$

where the non-local strain $\bar{\epsilon}$ is computed from

$$\bar{\epsilon}(\mathbf{x}) = \frac{1}{\Psi(\mathbf{x})} \int_{\Omega} \psi(\mathbf{y}, \mathbf{x}) \tilde{\epsilon}(\mathbf{y}) \mathrm{d}\Omega, \quad \Psi(\mathbf{x}) = \int_{\Omega} \psi(\mathbf{y}, \mathbf{x}) \mathrm{d}\Omega \tag{67}$$

with $\psi(\mathbf{y}, \mathbf{x})$, a weight function. Often, the weight function is assumed to be homogeneous and isotropic, so that it only depends on the norm $s = \| \mathbf{x} - \mathbf{y} \|$. In this formulation, all the other relations remain local: the local stress–strain relation (57), the loading–unloading conditions (59), and the dependence of the damage variable ω on the history parameter κ: $\omega = \omega(\kappa)$. As an alternative to Eq. (67), the locally defined history parameter κ may be replaced in the damage-loading function f by a spatially averaged quantity $\bar{\kappa}$:

$$\bar{\kappa}(\mathbf{x}) = \frac{1}{\Psi(\mathbf{x})} \int_{\Omega} \psi(\mathbf{y}, \mathbf{x}) \kappa(\mathbf{y}) \mathrm{d}\Omega \tag{68}$$

The fact that in elasticity-based damage models the stress can be computed directly from the given strain enables that a straightforward algorithm can be set up for non-local damage models.

Non-local constitutive relations can be considered as a point of departure for constructing gradient models, although it is emphasised that the latter class of models can also be defined directly by supplying
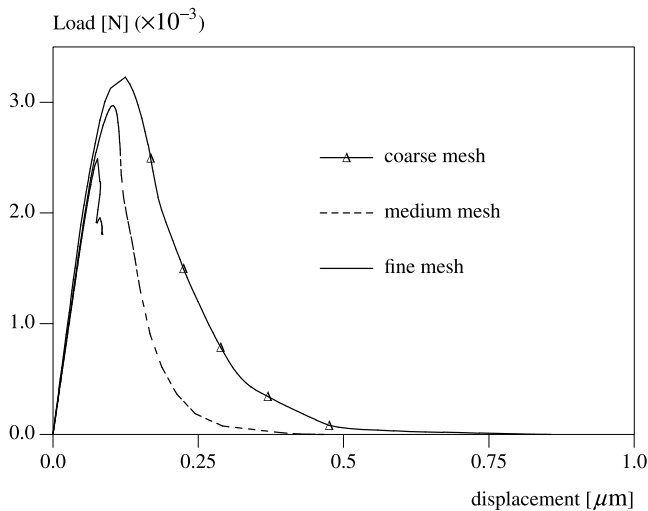
Fig. 19. Load–displacement curves for SiC/C specimen obtained with three different discretisations and a standard softening plasticity model [91].

higher-order gradients in the damage-loading function. Yet, we will follow the first-mentioned route to underline the connection between integral- and differential-type non-local models. This is done either by expanding the kernel $\tilde{\epsilon}$ of the integral in Eq. (67) in a Taylor series, or by expanding of the history parameter κ in Eq. (68) in a Taylor series. We will here consider the expansion of $\tilde{\epsilon}$, and refer to [94] for κ. If we truncate after the second-order terms and carry out the integration implied in (67) under the assumption of isotropy, the following relation ensues:

$$\bar{\epsilon} = \tilde{\epsilon} + c_g \nabla^2 \tilde{\epsilon} \tag{69}$$

where c_g is a gradient parameter of the dimension length squared. It can be related to the averaging volume and then becomes dependent on the precise form of the weight function ψ. For instance, for a one-dimensional continuum and taking

$$\psi(s) = \frac{1}{\sqrt{2\pi l}} e^{-s^2/2\ell^2} \tag{70}$$

we obtain $c_g = 1/2\ell^2$. Here, we adopt the phenomenological view that $\ell = \sqrt{(2c_g)}$ reflects the length scale of the failure process which we wish to describe macroscopically.

Formulation (69) has a disadvantage when applied in a finite element context, namely, that it requires computation of second-order gradients of the local equivalent strain $\tilde{\epsilon}$. Since this quantity is a function of the strain tensor, and since the strain tensor involves first-order derivatives of the displacements, third-order derivatives of the displacements have to be computed, which would necessitate C^2-continuity of the shape functions. To obviate this problem, Eq. (69) is differentiated twice and the result is substituted again into Eq. (69). Again neglecting fourth-order terms leads to

$$\bar{\epsilon} - c_g \nabla^2 \bar{\epsilon} = \tilde{\epsilon} \tag{71}$$

In [95], it has been shown that the implicit gradient formulation (71) becomes formally identical to a fully non-local formulation for a specific choice of the weighting function ψ in Eq. (67), which underlines that this formulation has a truly non-local character, in contrast to the explicit gradient formulation (69).

Higher-order continua require additional boundary conditions. With equation (71) governing the damage process, either the averaged equivalent strain $\bar{\epsilon}$ itself or its normal derivative must be specified on the boundary Γ of the body:

$$\bar{\epsilon} = \bar{\epsilon}_s \quad \text{or} \quad \mathbf{n}_\Gamma \cdot \nabla \bar{\epsilon} = \bar{\epsilon}_{ns} \tag{72}$$

In most example calculations in the literature, the natural boundary condition $\mathbf{n}_\Gamma \cdot \nabla \bar{\epsilon} = 0$ has been adopted.

Numerical schemes for gradient-enhanced continua typically have the character of a coupled problem and normally depart from the weak form of the balance of momentum:

$$\int_\Omega \nabla^{\text{sym}} \boldsymbol{\eta} : \boldsymbol{\sigma} \mathrm{d}\Omega = \int_\Gamma \boldsymbol{\eta} \cdot \mathbf{t}_p \mathrm{d}\Gamma \tag{73}$$

and a weak form of the averaging equation, for example, for Eq. (71):

$$\int_\Omega \zeta(\bar{\epsilon} - c_g \nabla^2 \bar{\epsilon} - \tilde{\epsilon}) \mathrm{d}\Omega = 0 \tag{74}$$

with ζ being the test function for the non-local strain $\bar{\epsilon}$. Transforming equation (74), using the divergence theorem and the natural boundary condition $\mathbf{n}_\Gamma \cdot \nabla \bar{\epsilon} = 0$ yields

$$\int_\Omega (\zeta \bar{\epsilon} + c_g \nabla \zeta \cdot \nabla \bar{\epsilon}) \mathrm{d}\Omega = \int_\Omega \zeta \tilde{\epsilon} \, \mathrm{d}\Omega \tag{75}$$

From Eq. (75) it becomes clear that in this formulation a C^0-interpolation for $\bar{\epsilon}$ suffices. Accordingly, we can discretise the displacements $\mathbf{u}$ and the non-local strains

$$\mathbf{u} = \mathbf{N}\mathbf{a} \quad \text{and} \quad \bar{\epsilon} = \bar{\mathbf{N}}\mathbf{e} \tag{76}$$

with $\mathbf{N}$ and $\bar{\mathbf{N}}$ containing C^0-interpolation polynomials, which can differ. Similarly, for the test functions

$$\boldsymbol{\eta} = \mathbf{N}\mathbf{w} \quad \text{and} \quad \zeta = \bar{\mathbf{N}}\mathbf{z} \tag{77}$$

Substitution into Eqs. (73) and (75) and requiring that the result holds for arbitrary $(\mathbf{w}, \mathbf{z})$, yields the discrete format of the equilibrium equation:

$$\int_\Omega \mathbf{B}^{\mathrm{T}} \boldsymbol{\sigma} \mathrm{d}\Omega = \int_\Gamma \mathbf{N}^{\mathrm{T}} \mathbf{t}_p \, \mathrm{d}\Gamma$$

and the averaging equation:

$$\int_\Omega (\bar{\mathbf{N}}^{\mathrm{T}} \bar{\mathbf{N}} + c_g (\nabla \bar{\mathbf{N}})^{\mathrm{T}} \nabla \bar{\mathbf{N}}) \mathrm{d}\Omega = \int_\Omega \bar{\mathbf{N}}^{\mathrm{T}} \tilde{\epsilon} \, \mathrm{d}\Omega \tag{78}$$

The tangent stiffness matrix needed for an iterative solution via the Newton–Raphson method reads [96] as follows:

$$\begin{bmatrix} \mathbf{K}_{aa} & \mathbf{K}_{ae} \\ \mathbf{K}_{ea} & \mathbf{K}_{ee} \end{bmatrix} \begin{pmatrix} \mathrm{d}\mathbf{a} \\ \mathrm{d}\mathbf{e} \end{pmatrix} = \begin{pmatrix} \mathbf{f}_a^{\text{ext}} - \mathbf{f}_a^{\text{int}} \\ \mathbf{f}_e^{\text{int}} - \mathbf{K}_{ee}\mathbf{e} \end{pmatrix} \tag{79}$$

with $\mathbf{f}_e^{\text{int}}$ given by the right-hand side of Eq. (78). The stiffness matrices are given by

$$\mathbf{K}_{aa} = \int_\Omega (1 - \omega)\mathbf{B}^{\mathrm{T}} \mathbf{D}^e \mathbf{B} \mathrm{d}\Omega \tag{80}$$

$$\mathbf{K}_{ae} = \int_\Omega q\mathbf{B}^{\mathrm{T}} \mathbf{D}^e \boldsymbol{\epsilon} \bar{\mathbf{N}} \mathrm{d}\Omega \tag{81}$$

$$\mathbf{K}_{ea} = \int_\Omega \bar{\mathbf{N}}^{\mathrm{T}} \left(\frac{\partial \tilde{\epsilon}}{\partial \boldsymbol{\epsilon}} \right) \mathbf{B} \mathrm{d}\Omega \tag{82}$$

$$\mathbf{K}_{ee} = \int_\Omega \left(\bar{\mathbf{N}}^{\mathrm{T}} \bar{\mathbf{N}} + c_g (\nabla \bar{\mathbf{N}})^{\mathrm{T}} \nabla \bar{\mathbf{N}} \right) \mathrm{d}\Omega \tag{83}$$

where $q = \partial\omega/\partial\kappa$ for loading and vanishes if otherwise. The expressions for $\mathbf{K}_{ae}$ and $\mathbf{K}_{ea}$ exhibit a non-symmetry. However, this non-symmetry is caused by the damage formalism and not by the gradient enhancement.

To illustrate the ability of gradient-enhanced damage models to accurately simulate fracture patterns, the Single-Edge Notched beam has again been chosen. The gradient-damage model outlined in the preceding has been used with material parameters, dimensions and boundary conditions as given in [97]. Fig. 20 shows an excellent agreement between the damage contours that result from the simulation and the experimentally observed crack pattern.
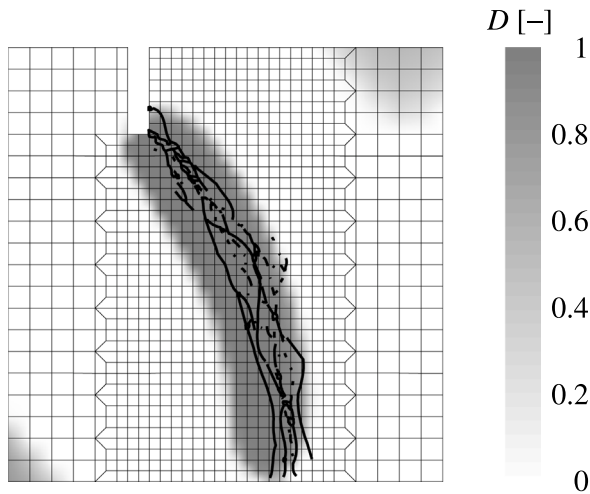
Fig. 20. Damage contours and experimentally observed crack patterns for the Single-Edge Notched beam using a gradient-enhanced damage model [97]. Only the centre part of the beam is shown.

5.5. The phase-field approach to brittle fracture

The central idea in the phase-field approximation to brittle fracture is the replacement of the Dirac function $\delta(x_n)$ by an approximated or regularised function [9,10]:

$$\delta_\ell(x_n) = \frac{1}{2\ell} \exp\left(-\frac{|x_n|}{\ell}\right) \tag{84}$$

with $\ell > 0$ a length scale parameter. Evidently

$$\int_{-\infty}^{\infty} \delta_\ell(x_n)\mathrm{d}x_n = 1 \tag{85}$$

for arbitrary ℓ, and x_n is a coordinate normal to the crack.

An issue with the smeared Dirac function approximation, Eq. (84), is that the generalisation towards more dimensions is less obvious. Therefore, it is obtained implicitly through the solution of the boundary value problem

$$\begin{cases} d - 4\ell^2 \frac{\mathrm{d}^2 d}{\mathrm{d}x_n^2} = 0 & x_n \in \mathbb{R}\backslash 0 \\ d = 1 & x_n = 0 \\ d = 0 & x_n = \pm\infty \end{cases} \tag{86}$$

with $d(x_n) \in [0,1]$ a scalar field, which equals 1 at the centre of the discontinuity, i.e. for $x_n = 0$, and vanishes for $x_n = \pm\infty$. When $d(0) = 1$ is not imposed, solution of the differential equation (86) is equivalent to minimising

$$I(d) = \frac{1}{4} \int_\Omega \left(d^2 + 4\ell^2 \frac{\mathrm{d}d}{\mathrm{d}x_n} \right) \mathrm{d}V \tag{87}$$

Since $\mathrm{d}V = \Gamma \mathrm{d}x_n$, we have

$$I(e^{-|x_n|/\ell}) = \ell \Gamma \tag{88}$$

where the crack surface can be expressed through the following volume integral:

$$\Gamma = \int_\Omega \gamma_\ell \mathrm{d}V \tag{89}$$

with the crack density

$$\gamma_\ell = \left(\frac{1}{4\ell} d^2 + \ell \|\nabla d\|^2 \right) \tag{90}$$

which is the multi-dimensional generalisation of $\delta_\ell(x_n)$.

We now consider a volume Ω with an internal discontinuity boundary Γ_d and we consider the potential energy for brittle fracture in the Griffith sense [2,8]:

$$\Psi_{\mathrm{pot}} = \int_\Omega \psi^e(\varepsilon) \mathrm{d}V + \int_{\Gamma_d} \mathcal{G}_c \mathrm{d}A \tag{91}$$

with the elastic energy density $\psi^e(\varepsilon)$ a function of the strain tensor ε. The elastic energy density is expressed by Hooke's law for an isotropic linear elastic material as $\psi^e(\varepsilon) = \frac{1}{2}\lambda\varepsilon_{ii}\varepsilon_{jj} + \mu\varepsilon_{ij}\varepsilon_{ij}$ with λ and μ the Lamé constants, and the summation convention applies. The potential energy Ψ_{pot} governs the balance between elastic energy in the bulk material and the fracture energy.

Next, the a priori unknown crack surface is approximated by the crack density function γ_ℓ, cf. Eqs. (89) - (90). This allows us to express the work required to create a unit crack area as a volume integral which depends on the phase field variable d and the fracture energy $\mathcal{G}_c$:

$$\int_{\Gamma_d} \mathcal{G}_c \mathrm{d}A = \int_\Omega \mathcal{G}_c \gamma_\ell(d, \nabla d) \mathrm{d}V \tag{92}$$

The final step is inspired by concepts developed in damage mechanics and relies on the assumption that the evolution of the phase field is directly related to crack growth. As such it can be used to model the loss of stiffness of the bulk of the solid. This is achieved by the introduction of a degradation function $g = g(d)$. A quadratic polynomial is widely used:

$$g(d) = (1 - d)^2 \tag{93}$$

but, motivated by work of Lorentz on gradient-damage models [98,99], a rational function has gained popularity more recently

$$g(d) = \frac{(1 - d)^2}{(1 - d)^2 + md(1 + pd)} \tag{94}$$

with m and p material parameters. The latter degradation function has been shown to be able to mimic cohesive-like behaviour, e.g. [100–102]. The degradation function g is then multiplied with the elastic energy density of the undamaged state, ψ_0, such that the elastic energy density of the damaged state reads [9]:

$$\psi^e(\varepsilon, d) = g(d)\psi_0(\varepsilon) \tag{95}$$

Noting that fracture occurs mainly in tension, it was subsequently assumed that the elastic energy of the undamaged state can be additively decomposed into a tensile or damage contribution, and an compressive or intact part, $\psi_0 = \psi_0^{\mathrm{d}} + \psi_0^{\mathrm{i}}$, and that the degradation function $g(d)$ only acts on the damaged part [103]:

$$\psi^e(\varepsilon, d) = g(d)\psi_0^{\mathrm{d}}(\varepsilon) + \psi_0^{\mathrm{i}}(\varepsilon) \tag{96}$$

Substituting Eqs. (92) and (96) into Eq. (91) yields the smeared form of the total potential energy for brittle fracture:

$$\Psi = \int_\Omega g(d)\psi_0^{\mathrm{d}}(\varepsilon) + \psi_0^{\mathrm{i}}(\varepsilon) + \mathcal{G}_c \gamma_l(d, \nabla d) \mathrm{d}V \tag{97}$$

Minimisation of Ψ and introduction of the history field $\mathcal{H}$ to enforce irreversibility [104] lead to the strong form:

$$\nabla \cdot \boldsymbol{\sigma}(\epsilon, d) = \mathbf{0} \qquad\qquad \mathbf{x} \in \Omega \tag{98a}$$

$$\boldsymbol{\sigma} \cdot \mathbf{n} = \bar{\mathbf{t}} \qquad\qquad \mathbf{x} \in \Gamma_t \tag{98b}$$

$$\mathbf{u} = \bar{\mathbf{u}} \qquad\qquad \mathbf{x} \in \Gamma_u \tag{98c}$$

$$\mathcal{G}_c \left(\frac{d}{2\ell^2} - 2\Delta d \right) = \frac{\mathrm{d}g(d)}{\mathrm{d}d}\mathcal{H} \qquad\qquad \mathbf{x} \in \Omega \tag{98d}$$

$$\nabla d \cdot \mathbf{n} = 0 \qquad\qquad \mathbf{x} \in \Gamma \tag{98e}$$

where $\bar{\mathbf{t}}$ and $\bar{\mathbf{u}}$ are the prescribed boundary tractions and displacements, respectively. The Cauchy stress $\boldsymbol{\sigma}$ and the history field $\mathcal{H}$ read:

$$\boldsymbol{\sigma}(\epsilon, d) = g(d)\frac{\partial\psi_0^{\mathrm{d}}}{\partial\epsilon} + \frac{\partial\psi_0^{\mathrm{i}}}{\partial\epsilon} \tag{99}$$

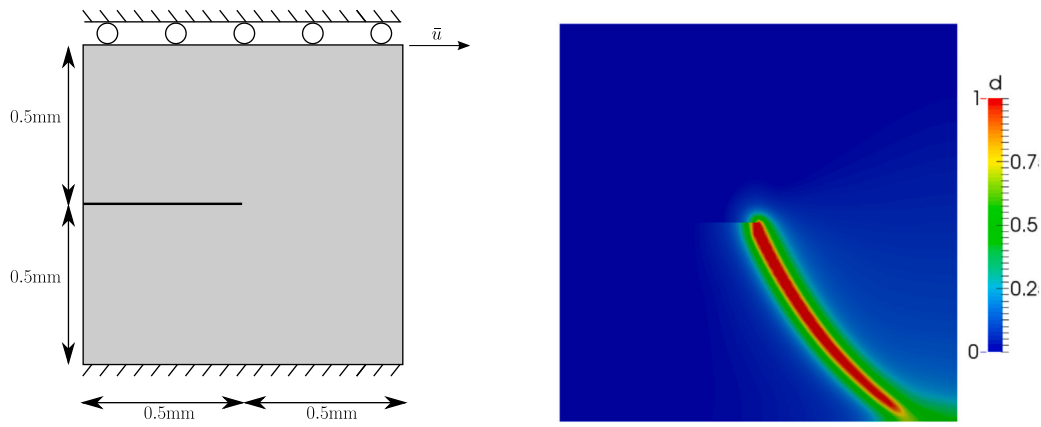$$\mathcal{H}(t) = \max_t \psi_0^{\mathrm{d}}(t). \tag{100}$$

Fig. 21. Notched plate. Left: geometry and boundary conditions. Right: Contours of the phase field.

The weak form of Eq. (98) can be derived in a standard fashion. The finite element approximation of the domain problem involves the following approximations of the field variables and their derivatives:

$$\begin{cases} \mathbf{u}(\mathbf{x}) = \mathbf{N}_u(\mathbf{x})\mathbf{u}^e \\ d(\mathbf{x}) = \mathbf{N}_d(\mathbf{x})\mathbf{d}^e \end{cases} \quad \begin{cases} \boldsymbol{\epsilon}(\mathbf{x}) = \mathbf{B}_u(\mathbf{x})\mathbf{u}^e \\ \dfrac{\partial d(\mathbf{x})}{\partial \mathbf{x}} = \mathbf{B}_d(\mathbf{x})\mathbf{d}^e \end{cases} \tag{101}$$

Substitution of these approximations into the weak form of Eq. (98d) leads to the following set of algebraic coupled equations:

$$\int_\Omega \mathbf{B}_u^{\mathrm{T}} \left(g(d)\mathbf{D}^{\mathrm{d}} + \mathbf{D}^{\mathrm{i}} \right) \mathbf{B}_u \mathbf{u}^e \, \mathrm{d}V = \mathbf{f}^{\text{ext}} \tag{102a}$$

$$\int_\Omega \left[\mathcal{G}_c \left(\frac{1}{2\ell}\mathbf{N}_d^{\mathrm{T}}\mathbf{N}_d + 2\ell\mathbf{B}_d^{\mathrm{T}}\mathbf{B}_d \right) \mathbf{d}^e + \frac{\mathrm{d}g(d)}{\mathrm{d}d}\mathcal{H}\mathbf{N}_d^{\mathrm{T}} \right] \mathrm{d}V = \mathbf{0} \tag{102b}$$

where $\mathbf{f}^{\text{ext}}$ is the external load vector, and $\mathbf{D}^{\mathrm{d}}$ and $\mathbf{D}^{\mathrm{i}}$ correspond to the damaged and intact parts of the elasticity matrix, respectively. The solution of the coupled set, Eqs. (102), is usually done using a staggered scheme, cf. [104], but there are indications that this can be at the expense of accuracy and that very fine load steps are needed to match the accuracy of monolithic schemes [105].

As an example a notched square plate of unit length, Fig. 21, is considered, which is subjected to a shear load, see [104,105] for details. The bottom edge is fixed, and the top edge is moved horizontally. The vertical displacements are prevented on the entire boundary, including on the initial notch. The results are given in Fig. 21 and were obtained using a monolithic scheme, a 100×100-element mesh of linear quadrilaterals, and a length scale $\ell = 0.02$ mm. The example shows that the brittle phase-field formulation is capable of predicting free crack propagation.

Phase-field methods have become very popular as a versatile, easy-to-implement method for simulating crack propagation, which obviates any need for complicated criteria for crack branching, and extends directly towards three dimensions. The meshes that are required, however, need to be dense, as several elements should fit in the specified internal length scale. This can lead to a huge demand on the computer run time for realistic structures. Also, the implementation of models which require the crack opening as input parameter, such as cohesive zone models, or transport of fluid in cracks, is problematic, since this parameter is not readily available. Several approaches have been suggested to repair this deficiency, such as augmenting the phase-field by an additional field that describes the crack opening [106], or reconstructing the crack opening from crack strains [107,108], but a fully robust solution does not seem to have been found yet.

6. Concluding remarks

In continuum modelling the smeared and discrete crack approaches have found strong supporters and adversaries, but it seems that the

evolution have made them grow closer. For instance, discrete crack modelling requires some form of discretisation adaptivity in order to produce physically realistic crack patterns. At the same time, advanced smeared methods like the phase-field approach require locally very dense meshes, which cannot be realised unless adaptivity is exploited. A major advantage of smeared methods is that they require less sophisticated data structures and that the extension to three dimensions is straightforward, which is not the case for discrete approaches. However, the proper implementation of models where a *crack opening* is an input parameter, such as cohesive-zone models or models in which fluid transport in cracks is considered, remains a challenge for smeared approaches, and this issue still awaits a thorough solution.

Declaration of competing interest

The authors declare that they have no known competing financial interests or personal relationships that could have appeared to influence the work reported in this paper.

Data availability

No data was used for the research described in the article.

Acknowledgement

References

[1] C.E. Inglis, Stresses in a plate due to the presence of cracks and sharp corners, Trans. Inst. Nav. Archit. 55 (1913) 219–241.
[2] A.A. Griffith, The phenomena of rupture and flow in solids, Philos. Trans. R. Soc. Lond. A221 (1921) 163–198.
[3] G. Irwin, Analysis of stresses and strains near the end of a crack traversing a plate, J. Appl. Mech. 24 (1957) 361–364.
[4] D.S. Dugdale, Yielding of steel sheets containing slits, J. Mech. Phys. Solids 8 (1960) 100–108.
[5] G.I. Barenblatt, The mathematical theory of equilibrium cracks in brittle fracture, Adv. Appl. Mech. 7 (1962) 55–129.
[6] D. Ngo, A.C. Scordelis, Finite element analysis of reinforced concrete beams, J. Am. Concr. Inst. 64 (1967) 152–163.
[7] Y.R. Rashid, Analysis of reinforced concrete pressure vessels, Nucl. Eng. Des. 7 (1968) 334–344.
[8] G.A. Francfort, J.J. Marigo, Revisiting brittle fracture as an energy minimization problem, J. Mech. Phys. Solids 46 (1998) 1319–1342.
[9] B. Bourdin, G.A. Francfort, J.J. Marigo, Numerical experiments in revisited brittle fracture, J. Mech. Phys. Solids 48 (2000) 797–826.
[10] B. Bourdin, G.A. Francfort, J.J. Marigo, The variational approach to fracture, J. Elasticity 91 (2008) 5–148.

[11] L. Chen, B. Li, R. de Borst, Adaptive isogeometric analysis for phase-field modeling of anisotropic brittle fracture, Internat. J. Numer. Methods Engrg. 121 (2020) 4630–4648.

[12] M.J. Borden, C.V. Verhoosel, M.A. Scott, T.J.R. Hughes, C.M. Landis, A phase-field description of dynamic brittle fracture, Comput. Methods Appl. Mech. Engrg. 217–220 (2012) 77–95.

[13] M.J. Borden, C.V. Verhoosel, M.A. Scott, T.J.R. Hughes, C.M. Landis, A higher-order phase-field model for brittle fracture: Formulation and analysis within the isogeometric analysis framework, Comput. Methods Appl. Mech. Engrg. 273 (2014) 100–118.

[14] R. de Borst, Computational Methods for Fracture in Porous Media, Elsevier, Amsterdam - Oxford - Cambridge (MA), 2018.

[15] R. Miller, M. Ortiz, R. Phillips, V. Shenoy, E.B. Tadmor, Quasicontinuum models of fracture and plasticity, Eng. Fract. Mech. 61 (1998) 427–444.

[16] S.J. Zhou, P.S. Lomdahl, A.F. Voter, B.L. Holian, Three-dimensional fracture via large-scale molecular dynamics, Eng. Fract. Mech. 61 (1998) 173–187.

[17] F.F. Abraham, R. Walkup, H. Gao, M. Duchaineau, T. Diaz De La Rubia, M. Seager, Simulating materials failure by using up to one billion atoms and the world's fastest computer: work-hardening, Proc. Natl. Acad. Sci. 99 (2002) 5783–5787.

[18] Z.S. Basinski, M.S. Duesberry, R. Taylor, Influence of shear stress on screw dislocations in a model sodium lattice, Can. J. Phys. 49 (1971) 2160–2180.

[19] J.F. Lutsko, Stress and elastic constants in anisotropic solids: molecular dynamics techniques, J. Appl. Phys. 64 (1988) 1152–1154.

[20] K.S. Cheung, S. Yip, Atomic-level stress in an inhomogeneous system, J. Appl. Phys. 70 (1991) 5688–5690.

[21] P.A. Cundall, O.D.L. Strack, A discrete numerical model for granular assemblies, Géotechnique 29 (1979) 47–65.

[22] N. Bićanić, Discrete element methods, in: Encyclopedia of Computational Mechanics Second Edition, John Wiley & Sons, Chichester, 2018, pp. 411–448.

[23] E. Schlangen, J.G.M. van Mier, Simple lattice model for numerical simulation of fracture of concrete materials and structures, Mater. Struct. 25 (1992) 534–542.

[24] E. Schlangen, E.J. Garboczi, Fracture simulations of concrete using lattice models: computational aspects, Eng. Fract. Mech. 57 (1997) 319–332.

[25] A.S.J. Suiker, A.V. Metrikine, R. de Borst, Comparison of wave propagation characteristics of the cosserat continuum model and corresponding discrete lattice models, Int. J. Solids Struct. 38 (2001) 1563–1583.

[26] P. Grassl, C. Fahy, D. Gallipoli, S.J. Wheeler, On a 2D hydro-mechanical lattice approach for modelling hydraulic fracture, J. Mech. Phys. Solids 75 (2015) 104–118.

[27] S. Kolhoff, P. Gumbsch, H.F. Frischmeister, Crack propagation in bcc crystals studied with a combined finite element and atomistic model, Phil. Mag. 64 (1991) 851–878.

[28] P. Aubertin, J. Réthoré, R. de Borst, Energy conservation of atomistic/continuum coupling, Internat. J. Numer. Methods Engrg. 78 (2009) 1365–1386.

[29] P. Aubertin, J. Réthoré, R. de Borst, Dynamic crack propagation using a combined molecular dynamics/extended finite element approach, Int. J. Multiscale Comput. Eng. 8 (2010) 221–235.

[30] P. Agrawal, B. Rice, D. Thompson, Predicting trends in rate parameters for self-diffusion on FCC metal surfaces, Surf. Sci. 515 (2009) 21–35.

[31] S. Nose, Constant-temperature molecular dynamics, J. Phys.: Condens. Matter. 2 (1990) 115–119.

[32] D. Broek, The Practical Use of Fracture Mechanics, Kluwer, Dordrecht, 1989.

[33] R.W. Hertzberg, Deformation and Fracture Mechanics of Engineering Materials, fourth ed., Wiley & Sons, New York, 1996.

[34] Z.P. Bažant, J. Planas, Fracture and Size Effect in Concrete and Other Quasibrittle Materials, CRC Press, Boca Raton, Florida, 1998.

[35] A. Hillerborg, M. Modéer, P.E. Petersson, Analysis of crack formation and crack growth in concrete by means of fracture mechanics and finite elements, Cem. Concr. Res. 6 (1976) 773–782.

[36] A. Needleman, A continuum model for void nucleation by inclusion of debonding, J. Appl. Mech. 54 (1987) 525–531.

[37] V. Tvergaard, J.W. Hutchinson, The relation between crack growth resistance and fracture process parameters in elastic-plastic solids, J. Mech. Phys. Solids 41 (1992) 1119–1135.

[38] H.W. Reinhardt, H.A.W. Cornelissen, Post-peak cyclic behaviour of concrete in uniaxial and alternating tensile and compressive loading, Cem. Concr. Res. 14 (1984) 263–270.

[39] J.W. Hutchinson, A.G. Evans, Mechanics of materials: top–down approaches to fracture, Acta Mater. 48 (2000) 125–135.

[40] N. Chandra, H. Li, C. Shet, H. Ghonem, Some issues in the application of cohesive zone models for metal-ceramic interfaces, Int. J. Solids Struct. 39 (2002) 2827–2855.

[41] S. Pietruszczak, Z. Mróz, Finite element analysis of deformation of strain softening materials, Internat. J. Numer. Methods Engrg. 17 (1981) 327–334.

[42] Z.P. Bažant, B. Oh, Crack band theory for fracture of concrete, RILEM Mater. Struct. 16 (1983) 155–177.

[43] J. Oliver, A consistent characteristic length for smeared cracking models, Internat. J. Numer. Methods Engrg. 28 (1989) 461–474.

[44] P.H. Feenstra, R. de Borst, A plasticity model for mode I cracking in concrete, Internat. J. Numer. Methods Engrg. 38 (1995) 2509–2529.

[45] M. Jirasek, M. Bauer, Numerical aspects of the crack band approach, Comput. Struct. 110 (2012) 60–78.

[46] J.G. Rots, Smeared and discrete representations of localized fracture, Int. J. Fract. 51 (1991) 45–59.

[47] A.R. Ingraffea, V. Saouma, Numerical modelling of discrete crack propagation in reinforced and plain concrete, in: Fracture Mechanics of Concrete, Martinus Nijhoff Publishers, Dordrecht, 1985, pp. 171–225.

[48] G.T. Camacho, M. Ortiz, Computational modelling of impact damage in brittle materials, Int. J. Solids Struct. 33 (1996) 2899–2938.

[49] B.A. Schrefler, S. Secchi, L. Simoni, On adaptive refinement techniques in multifield problems including cohesive fracture, Comput. Methods Appl. Mech. Engrg. 195 (2006) 444–461.

[50] S. Secchi, L. Simoni, B.A. Schrefler, Mesh adaptation and transfer schemes for discrete fracture propagation in porous materials, Int. J. Numer. Anal. Methods Geomech. 31 (2007) 331–345.

[51] M.G.A. Tijssens, L.J. Sluys, E. van der Giessen, Numerical simulation of quasi-brittle fracture using damaging cohesive surfaces, Eur. J. Mech.: A/Solids 19 (2000) 761–779.

[52] O. Allix, P. Ladevèze, Interlaminar interface modelling for the prediction of delamination, Compos. Struct. 22 (1992) 235–242.

[53] J.C.J. Schellekens, R. de Borst, A non-linear finite element approach for the analysis of mode-I free edge delamination in composites, Int. J. Solids Struct. 30 (1993) 1239–1253.

[54] J.C.J. Schellekens, R. de Borst, Free edge delamination in carbon-epoxy laminates: a novel numerical/experimental approach, Compos. Struct. 28 (1994) 357–373.

[55] O. Allix, A. Corigliano, Geometrical and interfacial non-linearities in the analysis of delamination in composites, Int. J. Solids Struct. 36 (1999) 2189–2216.

[56] X.P. Xu, A. Needleman, Numerical simulations of fast crack growth in brittle solids, J. Mech. Phys. Solids 42 (1994) 1397–1434.

[57] P. Krysl, T. Belytschko, The element-free Galerkin method for dynamic propagation of arbitrary 3-D cracks, Internat. J. Numer. Methods Engrg. 44 (1999) 767–800.

[58] B. Nayroles, G. Touzot, P. Villon, Generalizing the finite element method: diffuse approximations and diffuse elements, Comput. Mech. 10 (1992) 307–318.

[59] T. Belytschko, Y. Lu, L. Gu, Element-free Galerkin methods, Internat. J. Numer. Methods Engrg. 37 (1994) 229–256.

[60] P. Lancaster, K. Salkauskas, Surfaces generated by moving least squares, Math. Comp. 37 (1981) 141–158.

[61] M. Fleming, Y.A. Chu, B. Moran, T. Belytschko, Enriched element-free Galerkin methods for crack tip fields, Internat. J. Numer. Methods Engrg. 40 (1997) 1482–1504.

[62] D. Hegen, Element-free Galerkin methods in combination with finite element approaches, Comput. Methods Appl. Mech. Engrg. 135 (1996) 143–166.

[63] T. Belytschko, T. Black, Elastic crack growth in finite elements with minimal remeshing, Internat. J. Numer. Methods Engrg. 45 (1999) 601–620.

[64] N. Moës, J. Dolbow, T. Belytschko, A finite element method for crack growth without remeshing, Internat. J. Numer. Methods Engrg. 46 (1999) 131–150.

[65] I. Babuška, J.M. Melenk, The partition of unity method, Internat. J. Numer. Methods Engrg. 40 (1997) 727–758.

[66] T. Strouboulis, I. Babuška, K. Copps, The design and analysis of the generalized finite element method, Comput. Methods Appl. Mech. Engrg. 181 (2000) 43–69.

[67] G.N. Wells, L.J. Sluys, A new method for modelling cohesive cracks using finite elements, Internat. J. Numer. Methods Engrg. 50 (2001) 2667–2682.

[68] J.J.C. Remmers, R. de Borst, A. Needleman, A cohesive segments method for the simulation of crack growth, Comput. Mech. 31 (2003) 69–77.

[69] J.J.C. Remmers, R. de Borst, A. Needleman, The simulation of dynamic crack propagation using the cohesive segments method, J. Mech. Phys. Solids 56 (2008) 70–92.

[70] T.J.R. Hughes, J.A. Cottrell, Y. Bazilevs, Isogeometric analysis: CAD, finite elements, NURBS, exact geometry and mesh refinement, Comput. Methods Appl. Mech. Engrg. 194 (2005) 4135–4195.

[71] Y. Bazilevs, V.M. Calo, J.A. Cottrell, J.A. Evans, T.J.R. Hughes, S. Lipton, M.A. Scott, T.W. Sederberg, Isogeometric analysis using T-splines, Comput. Methods Appl. Mech. Engrg. 199 (2010) 229–263.

[72] M.G. Cox, The numerical evaluation of B-splines, IMA J. Appl. Math. 10 (1972) 134–149.

[73] C. de Boor, On calculating with B-splines, J. Approx. Theory 6 (1972) 50–62.

[74] C.V. Verhoosel, M.A. Scott, R. de Borst, T.J.R. Hughes, An isogeometric analysis approach to cohesive zone modelling, Internat. J. Numer. Methods Engrg. 87 (2011) 336–360.

[75] S. May, J. Vignollet, R. de Borst, Powell-Sabin B-splines and unstructured standard T-splines for the solution of Kichhoff-Love plate theory using Bézier extraction, Internat. J. Numer. Methods Engrg. 107 (2016) 205–233.

[76] F. Irzal, J.J.C. Remmers, C.V. Verhoosel, R. de Borst, Isogeometric finite element analysis of poroelasticity, Int. J. Numer. Anal. Methods Geomech. 37 (2013) 1891–1907.

[77] J. Lemaitre, J.L. Chaboche, Mechanics of Solids Materials, Cambridge University Press, 1990.

[78] H. Askes, J. Pamin, R. de Borst, Dispersion analysis and element-free Galerkin solutions of second-and fourth-order gradient-enhanced damage models, Internat. J. Numer. Methods Engrg. 49 (2000) 811–832.

[79] C.V. Verhoosel, M.A. Scott, T.R. Hughes, R. de Borst, An isogeometric analysis approach to gradient damage models, Internat. J. Numer. Methods Engrg. 86 (2011) 115–134.

[80] R. Cope, P.V. Rao, L.A. Clark, P. Norris, Modelling of reinforced concrete behaviour for finite element analysis of bridge slabs, in: C. Taylor, E. Hinton, D.R.J. Owen (Eds.), Numerical Methods for Non-Linear Problems, Pineridge Press, Swansea, 1980, pp. 457–470.

[81] M. Suidan, W.C. Schnobrich, Finite element analysis of reinforced concrete, ASCE J. Struct. Div. 99 (1973) 2109–2122.

[82] R. de Borst, Computation of post-bifurcation and post-failure behaviour of strain-softening solids, Comput. Struct. 25 (1987) 221–224.

[83] M. Ortiz, Y. Leroy, A. Needleman, A finite element method for localized failure analysis, Comput. Methods Appl. Mech. Engrg. 61 (1987) 189–214.

[84] T. Belytschko, J. Fish, B.E. Engelman, A finite element with embedded localization zones, Comput. Methods Appl. Mech. Engrg. 70 (1988) 59–89.

[85] J.C. Simo, J. Oliver, F. Armero, An analysis of strong discontinuities induced by softening relations in rate-independent solids, Comput. Mech. 12 (1993) 277–296.

[86] R. de Borst, G.N. Wells, L.J. Sluys, Some observations on embedded discontinuity models, Eng. Comput. 18 (2001) 241–254.

[87] R.I. Borja, A finite element model for strain localization analysis of strongly discontinuous fields based on standard Galerkin approximation, Comput. Methods Appl. Mech. Engrg. 190 (2000) 1529–1549.

[88] R. de Borst, M. Gutierrez, A unified framework for concrete damage and fracture models including size effects, Int. J. Fract. 95 (1999) 261–277.

[89] J. Mazars, G. Pijaudier-Cabot, Continuum damage theory – application to concrete, ASCE J. Eng. Mech. 115 (1989) 345–365.

[90] J.H.P. de Vree, W.A.M. Brekelmans, M.A. van Gils, Comparison of nonlocal approaches in continuum damage mechanics, Comput. Struct. 55 (1995) 581–588.

[91] R. de Borst, Some recent issues in computational failure mechanics, Internat. J. Numer. Methods Engrg. 52 (2001) 63–95.

[92] J. Pamin, H. Askes, R. de Borst, Two gradient plasticity theories discretized with the element-free Galerkin method, Comput. Methods Appl. Mech. Engrg. 192 (2003) 3391–3403.

[93] G. Pijaudier-Cabot, Z.P. Bažant, Nonlocal damage theory, ASCE J. Eng. Mech. 113 (1987) 1512–1533.

[94] R. de Borst, C.V. Verhoosel, Gradient damage vs phase-field approaches for fracture: Similarities and differences, Comput. Methods Appl. Mech. Engrg. 312 (2016) 78–94.

[95] R.H.J. Peerlings, M.G.D. Geers, R. de Borst, W.A.M. Brekelmans, A critical comparison of nonlocal and gradient-enhanced softening continua, Int. J. Solids Struct. 38 (2001) 7723–7746.

[96] R.H.J. Peerlings, R. de Borst, W.A.M. Brekelmans, H.P.J. de Vree, Gradient-enhanced damage for quasi-brittle materials, Internat. J. Numer. Methods Engrg. 38 (1996) 3391–3403.

[97] R.H.J. Peerlings, R. de Borst, W.A.M. Brekelmans, M.G.D. Geers, Gradient-enhanced damage modelling of concrete fracture, Mech. Cohesive-Frictional Mater. 3 (1998) 323–342.

[98] E. Lorentz, S. Cuvilliez, K. Kazymyrenko, Modelling large crack propagation: from gradient damage to cohesive zone models, Int. J. Fract. 178 (2012) 85–95.

[99] E. Lorentz, A nonlocal damage model for plain concrete consistent with cohesive fracture, Int. J. Fract. 207 (2017) 123–159.

[100] J.Y. Wu, A unified phase-field theory for the mechanics of damage and quasi-brittle failure, J. Mech. Phys. Solids 103 (2017) 72–99.

[101] R.J.M. Geelen, Y. Liu, T. Hu, M.R. Tupek, J.E. Dolbow, A phase-field formulation for dynamic cohesive fracture, Comput. Methods Appl. Mech. Engrg. 348 (2019) 680–711.

[102] L. Chen, R. de Borst, Phase-field modelling of cohesive fracture, Eur. J. Mech.: A/Solids 90 (2021) 104343.

[103] H. Amor, J.-J. Marigo, C. Maurini, Regularized formulation of the variational brittle fracture with unilateral contact: Numerical experiments, J. Mech. Phys. Solids 57 (2009) 1209–1229.

[104] C. Miehe, M. Hofacker, F. Welschinger, A phase field model for rate-independent crack propagation: Robust algorithmic implementation based on operator splits, Comput. Methods Appl. Mech. Engrg. 199 (2010) 2765–2778.

[105] J. Vignollet, S. May, R. de Borst, C.V. Verhoosel, Phase-field models for brittle and cohesive fracture, Meccanica 49 (2014) 2587–2601.

[106] C.V. Verhoosel, R. de Borst, A phase-field model for cohesive fracture, Internat. J. Numer. Methods Engrg. 96 (2013) 43–62.

[107] T.T. Nguyen, J. Yvonnet, Q.Z. Zhu, M. Bornert, C. Chateau, A phase-field method for computational modeling of interfacial damage interacting with crack propagation in realistic microstructures obtained by microtomography, Comput. Methods Appl. Mech. Engrg. 312 (2016) 567–595.

[108] C. Chukwudozie, B. Bourdin, K. Yoshioka, A variational phase-field model for hydraulic fracturing in porous media, Comput. Methods Appl. Mech. Engrg. 347 (2019) 957–982.